Max-Planck-Institut für Meteorologie

REPORT No. 55

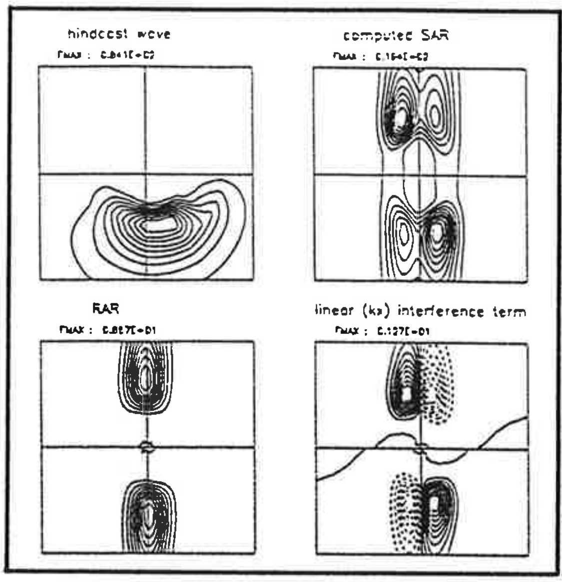

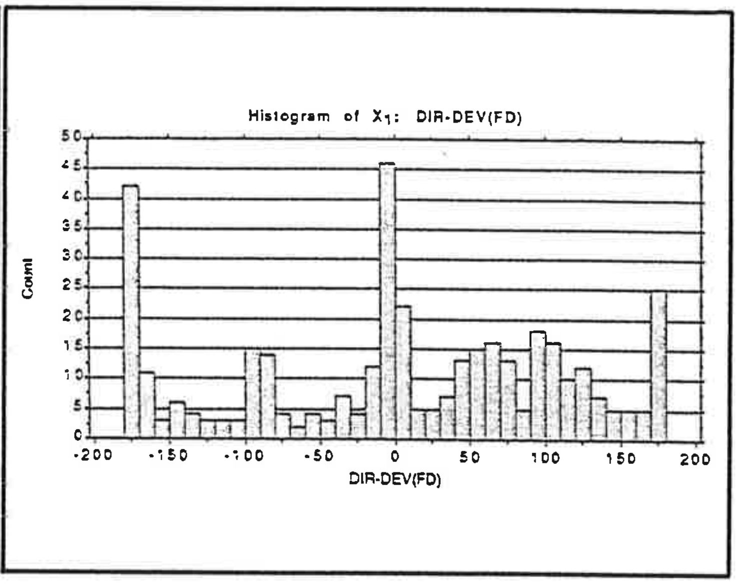

EUROPEAN SPACE AGENCY CONTRACT REPORT

USE OF A WAVE MODEL AS A VALIDATION TOOL FOR ERS-1 AMI WAVE PRODUCTS AND AS AN INPUT FOR THE ERS-1 WIND RETRIEVAL ALGORITHMS

PART 1 ON THE NONLINEAR MAPPING OF AN OCEAN WAVE SPECTRUM INTO A SAR IMAGE SPECTRUM AND ITS INVERSION

PART 2 STUDY OF THE IMPACT OF THE SURFACE WAVE FIELD ON THE C-BAND MODEL FUNCTION AND THE DERIVED WIND VECTOR

AUTHORS

K. Hasselmann
S. Hasselmann
K. Barthel

ESRIN CONTRACT NO:
7851/88/HGE-I

ESRIN STUDY MANAGER
E. ORIOL

HAMBURG, AUGUST 1990

AUTHORS:

KLAUS HASSELMANN — MAX-PLANCK-INSTITUT
SUSANNE HASSELMANN — FUER METEOROLOGIE

KNUT BARTHEL — NANSEN REMOTE SENSING CENTER
EDVARD GRIEGSVEI 3a
N-5037 SOLHEIMSVIKEN

Sections 1-5, 7 and Appendix of Part 1
of this manuscript constitutes a paper by K. Hasselmann and S. Hasselmann
'On the nonlinear mapping of an ocean wave spectrum
into a SAR image spectrum and its inversion',
which has been submitted for publication to the Journal of Geophysical Research, Oceans

Section 6 of Part 1
is included in a paper by K. Hasselmann, S. Hasselmann, C. Brüning and A. Speidel
'Application of a new closed ocean wave-SAR spectral
transform relation to LEWEX data',
to appear in the Proceedings of the conference on 'Directional Ocean Wave Spectra', April 18-20, 1989, the Johns Hopkins University, Laurel, Maryland, USA

Acknowledgements

In addition to the support by ESA, the work carried out in this contract was partly supported the US Office of Naval Research under Contract No. N00014-88-J-1025

MAX-PLANCK-INSTITUT
FUER METEOROLOGIE
BUNDESSTRASSE 55
D-2000 HAMBURG 13
F.R. GERMANY

Tel.: (040) 4 11 73-0
Telex: 211092
Telemail: MPI.METEOROLOGY
Telefax: (040) 4 11 73-298

REPb55

ISSN 0937-1060

ESA STUDY CONTRACT REPORT

No ESA Study Contract Report will be accepted unless this sheet is inserted at the beginning of each volume of the Report.

ESA CONTRACT NO 7851/88/ HGE-I	SUBJECT Use of a wave model as a validation tool for ERS-1 AMI wave products and as an input for the ERS-1 wind retrieval algorithms	NAME OF CONTRACTOR MPI
* ESA CR( ) No: 1	* STAR CODE	No. of Volumes 1 This is Volume No: 1
		CONTRACTOR'S REFERENCE

ABSTRACT.

The principal conclusions of the study report may be summarized as follows:

1) The development of new closed integral transformation relation for the mapping of a surface wave spectrum into a SAR image spectrum initiated in the previous ESA study contract was successfully completed and implemented. It has been applied to SEASAT and LEWEX (Labrador Extreme Waves Experiment) spectra.

2) A general method for inverting the transformation was developed. It was successfully applied to determine wave spectra from SEASAT spectra, using WAM model hindcast wave spectra as a first guess.

3) A model of C-band microwave backscatter from the seasurface was developed which allows for the hydrodynamic interactions between the backscattering ripple waves and the long ocean wave spectrum.

4) Numerical simulations demonstrated a significant impact of the long wave spectrum on the scatterometer wind retrievals.

5) The ground work has now been established for implementing improved wind and wave retrieval algorithms from the ERS-1 AMI SAR wave mode and scatterometer data. This will require an integrated approach in which the sensor algorithms developed in this report are combined with the first guess wind and wave fields provided by atmospheric and global wave models. In a subsequent step, retrieved wind and wave data can then be assimilated in the models to provide the global gridded wind and wave fields required by the forecasting and research community.

Names of authors:

K. Hasselmann, S. Hasselmann, and K. Barthel

** NAME OF ESA STUDY MANAGER E Oriol DIV: OEE	** ESA BUDGET HEADING 65.512	

* Sections to be completed by ESA

** Information to be provided by ESA Study Manager

Max-Planck-Institut für Meteorologie
Bundesstraße 55, 2000 Hamburg 13, FRG

Report No.: 55

EUROPEAN SPACE AGENCY CONTRACT REPORT

USE OF A WAVE MODEL AS A VALIDATION TOOL FOR ERS-1 AMI WAVE PRODUCTS AND AS AN INPUT FOR THE ERS-1 WIND RETRIEVAL ALGORITHMS

K. Hasselmann (1)
S. Hasselmann (1)
K. Barthel (2)

ESRIN CONTRACT NO.:
7851/88/HGE-I

ESRIN STUDY MANAGER
E. Oriol

Part 1: On the nonlinear mapping of an ocean wave spectrum into a SAR image spectrum and its inversion.

K. Hasselmann
S. Hasselmann

Part 2: Study of the impact of the surface wave field on the C-band model function and the derived wind vector.

K. Barthel
K. Hasselmann

(1) Max-Planck-Institut für Meteorologie, Hamburg
(2) Nansen Remote Sensing Center, Bergen

Contents

Summary

The **purpose** of ESA study contract 7851/88/HGE-I, as defined in the **"Statement of work"**, was:

> The implementation of the theory developed in the previous study contract (Contract no. 6875/87/HGE-I) in order to allow the interpretation / validation of the SAR image spectrum by using as a first guess the wave spectrum obtained from a wave model. A step further should be to develop a method of optimisation in order to minimize the error between the locally computed SAR image spectrum (from the model) and observed SAR image spectrum to eventually derive the surface wave spectrum.
>
> The application of a generalized C-band model which includes the information of the wave field in the wind retrieval algorithm. Study of the impact of such approach.

The main **tasks** of the study contract were divided into the following three **work packages** (cf "statement of work").

WP 100
Computation of the SAR wave image spectrum from a prescribed surface wave spectrum using the theory developed in the previous study contract.

WP 110
Develop an efficient program applicable for an arbitrary two-dimensional wave spectrum as produced by a wave model. Evaluate the results in view of its operational use for the interpretation of SAR image spectra.

WP 120
Compute the impact of a perturbation of the surface wave spectrum on the SAR image spectrum.

Part 1, with the exception of Section 6, has been submitted for publication to the Journal of Geophysical Research. The results of Part 1, Section 6, have been presented at the Symposium on Ocean Wave Spectra at the Applied Physics Laboratory of Johns Hopkins University, 18-20 April 1990 and will be published in the proceedings of that meeting. The results of **Part 2** are also planned for publication.

Extended summaries (Part 1) and **conclusions** (Parts 1 and 2) are given in the two main parts of the report.

The **principal conclusions** of the study report may be summarized as follows:

1) The development of new closed integral transformation relation for the mapping of a surface wave spectrum into a SAR image spectrum initiated in the previous ESA study contract was successfully completed and implemented. It has been applied to SEASAT and LEWEX (Labrador Extreme Waves Experiment) spectra.

2) A general method for inverting the transformation was developed. It was successfully applied to determine wave spectra from SEASAT spectra, using WAM model hindcast wave spectra as a first guess.

3) A model of C-band microwave backscatter from the sea surface was developed which allows for the hydrodynamic interactions between the backscattering ripple waves and the long ocean wave spectrum.

4) Numerical simulations demonstrated a significant impact of the long wave spectrum on the scatterometer wind retrievals.

5) The ground work has now been established for implementing improved wind and wave retrieval algorithms from the ERS-1 AMI SAR wave mode and scatterometer data. This will

PART 1

On the nonlinear mapping of an ocean wave spectrum into a SAR image spectrum and its inversion

by

Klaus Hasselmann
Susanne Hasselmann

Abstract

A new closed nonlinear integral transformation relation is derived describing the mapping of a two-dimensional ocean wave spectrum into a Synthetic Aperture Radar (SAR) image spectrum. The general integral relation is expanded in a power series with respect to orders of nonlinearity and velocity bunching. The individual terms of the series can be readily computed using fast Fourier transforms. The convergence of the series is rapid. The series expansion is also useful in identifying the different contributions to the net imaging process, consisting of the real aperture radar (RAR) cross-section modulation, the nonlinear motion (velocity bunching) effects, and their various interaction products.

The lowest term of the expansion with respect to nonlinearity order yields a simple quasi-linear approximate mapping relation consisting of the standard linear SAR modulation expression multiplied by an additional nonlinear Gaussian azimuthal cut-off factor. The cut-off scale is given by the rms azimuthal (velocity bunching) displacement. The same cut-off factor applies to all terms of the power series expansion.

This situation could change dramatically in the nineties. We look forward in this decade to extensive, in some cases continuous, global measurements of the two-dimensional wave spectrum from Synthetic Aperture Radars flown on satellites such as ERS-1 and 2, RADARSAT, shuttle missions and polar platforms. These data will be augmented by global significant wave height measurements from radar altimeters on ERS-1, 2, Topex-Poseidon, Spinsat, and other satellites. Furthermore, global sea surface wind data from satellite scatterometers and altimeters will provide improved wind fields as input for wave models. The simultaneous assimilation of these wind and wave data into global wave models and atmospheric forecast models offers exciting new opportunities and perspectives for wave modellers - but also presents major challenges to the wave and weather forecasting community.

This is exemplified by the SAR wave data. The potential of space-borne SARs for imaging two-dimensional ocean wave fields from space has been convincingly demonstrated by SEASAT (cf. Alpers, 1983; Beal et al., 1983 and other papers in the SEASAT issue, Journal of Geophysical Research, Vol. **88**, 1983) and the shuttle SIR-B mission (cf. Alpers et al., 1986; Brüning et al., 1988; Monaldo and Lyzenga, 1988). The theory of the SAR imaging of a moving ocean wave surface is now also rather well understood (cf. MARSEN SAR review, Hasselmann et al., 1985, referred to in the following as MSR). The theory has been verified in a number of field experiments with air-borne SARs as well as in SEASAT and SIR-B hindcast studies. Nevertheless, the routine interpretation and application of SAR wave data is still generally regarded as a major unresolved problem because of the inherent complexities of the basically nonlinear imaging process.

A fundamental difficulty is that not all of the wave spectral information is mapped into the SAR image plane. Since SAR images provide only a snapshot of the instantaneous sea surface, they can determine the wave propagation direction only to within a sign. (The ambiguity can be removed in principle by correlating successive looks of the same scene, although this proposal - Rosenthal, Raney, private communication - has to our knowledge not yet been tested.) A more serious loss of information is incurred by the nonlinear distortion induced by motion effects. These result in an azimuthal high wavenumber cut-off of the spectrum. The nonlinearities also produce significant shifts of the spectral peak and other distortions of the spectrum (Alpers and Brüning, 1986; Brüning et al., 1988, 1990).

Most of these limitations, if properly understood, can be suitably dealt with if the SAR ocean wave image data are assimilated into a wave model. However, this is feasible only if there exists an accurate, operationally feasible method of computing the SAR image spectrum for a given wave spectrum, together with an associated technique for inverting the mapping relation. An essential first step towards the application of SAR wave data in wave models must therefore be the derivation of an efficient and accurate method for computing the mapping from a surface wave spectrum into a SAR surface image spectrum. Subsequently, a method must be devised for dealing with the loss of information incurred in the forward mapping relation and recovering the wave spectrum from the measured SAR image spectrum. Both of these questions are addressed in this paper.

Since the basic imaging mechanisms are known, a straightforward method of solving the forward mapping problem is to compute the SAR image for any given instantaneous realization of the sea surface pixel by pixel for each (moving) scattering element of the surface. Monte Carlo computations of the spectrum of the SAR image for a given two-dimensional wave spectrum using an ensemble of such deterministic mapping

Finally, with the availability of a closed, noise free, rapidly computable transformation expression, it is now possible to address the inverse problem of deriving the wave spectrum from the SAR spectrum. Because of the loss of information beyond the azimuthal cut-off and the 180° ambiguity, a rigorous inverse mapping solution does not exist. However, regularization can be achieved in the usual manner by minimizing a cost function which penalizes not only the deviation between the observed and predicted SAR spectrum, but also the deviation between the modified wave spectrum and a first-guess wave spectrum. The iterative inversion method developed in this paper generally converges within three or four iterations. The computations should be sufficiently rapid for application in an operational SAR data assimilation system.

The paper is structured as follows: Section 2 reviews the different imaging mechanisms and defines notation. The basic nonlinear mapping relation is derived in Section 3. Section 4 describes the inversion method. The results of Sections 3 and 4 are illustrated in Section 5 for three selected SAR images from SEASAT, taking as first guess input spectra the wave spectra derived from a global wave hindcast using the WAM 3rd generation wave model (WAMDIG, 1988). Further examples of the forward transform relation are given in Section 6 for two cases from LEWEX (Labrador Extreme Waves Experiment). Section 7, finally, summarizes the principal results and conclusions of the study. An appendix describes the generalization of the pure velocity bunching theory presented in Section 3 to higher order processes such as acceleration smearing.

is given in Section 6 for the [illegible] LEWEX [illegible]

Waves Experiment) [illegible]

For all processes it can be assumed that to first order the backscattering ripple waves and the modulating ocean waves are widely separated in wavelength scale. On the basis of this two-scale description, a rather complete theory of SAR imaging of a random ocean wave field can be developed (Alpers and Rufenach, 1979; Swift and Wilson, 1979; Valenzuela, 1980; Alpers et al., 1981; Raney, 1981; Tucker, 1985; MSR).

An important feature of the theory is that SAR imaging is typically nonlinear. Although the hydrodynamic and tilt modulation can usually be approximated as linear processes, the so called 'velocity bunching' mechanism associated with the orbital motion of the long waves is frequently strongly nonlinear, particularly for windseas and short waves. Velocity bunching arises through the variations in the azimuthal displacements of the imaged backscattering elements induced by the variations of the orbital velocity within the long wave field. The alternate bunching and stretching of the apparent scatterer distribution in the image plane produces an image of the long waves, even in the hypothetical case that the backscattering cross-section itself is not modulated. When the displacements are small compared with the characteristic wavelength of the long waves, the mechanism can be treated as a linear process, characterized by a velocity bunching modulation transfer function (MTF), in analogy with the hydrodynamic and tilt MTF's. For larger displacements, however, the process becomes nonlinear, and when the displacements significantly exceed a wavelength (for example, for short wind waves travelling in the azimuthal direction) the image can become completely smeared out.

In the following it will be convenient to regard the SAR wave image as produced by two consecutive imaging processes: the frozen surface (or real aperture radar, RAR) imaging mechanism, governed by the hydrodynamic derivative notation required for continuous integrals. The transition to continuous integrals is carried out at the end of the analysis.

For the general theory presented in the next section, $T_{\mathbf{k}}^{R}$ need not be further specified. However, for later numerical applications $T_{\mathbf{k}}^{R}$ needs to be evaluated in more detail by decomposition into its tilt and hydrodynamic modulation components,

$$T_{\mathbf{k}}^{R} = T_{\mathbf{k}}^{h} + T_{\mathbf{k}}^{t} \tag{2.4}$$

For a Phillips k^{-4} high wavenumber spectrum, the tilt MTF can be approximated for large dialectric constants (which for sea water are of the order of 80), by the expressions (cf. Wright, 1968; Lyzenga, 1986)

$$T^{t}(\mathbf{k}) = 4ik_{\ell} \begin{cases} \cot\theta \cdot (1+\sin^{2}\theta)^{-1} & \text{for vertical polarization } (VV) \\ & (\text{for } \theta \le 60^{\circ}) \\ 2\,(\sin 2\theta)^{-1} & \text{for horizontal polarization } (HH) \end{cases} \tag{2.5}$$

where θ is the radar incidence angle and k_{ℓ} the component of the incident wavenumber vector in the radar look direction.

The hydrodynamic MTF can be derived from a two-scale model of hydrodynamic short wave-long wave interactions. A simple relaxation type source term, characterized by a damping factor μ, is normally introduced to describe response of the short waves to the long wave modulation (cf. Keller and Wright, 1975). Feindt (1985) found that a better agreement to lie on the two free gravity wave dispersion surfaces $\omega = \pm \sqrt{gk}$. Thus in (2.1), (2.2) Fourier components of opposite sign in $\mathbf{k}$ represent different waves travelling in opposite directions, and are not related, in contrast to (2.7), where the components are related through (2.8). (For the same reason, eqns (2.1), (2.2) include a second explicit complex conjugate sum, whereas in (2.7) the complex conjugate wavenumber pairs are already included implicitly in the single sum over positive and negative $\mathbf{k}$.)

For a RAR, the image intensity is directly proportional to the specific cross-section. Thus if the image modulation is normalized by the mean image intensity, we have

$$I^R(\mathbf{r}) \equiv \sigma\,(\mathbf{r},0)/\bar{\sigma} - 1 \qquad (2.9)$$

and equations (2.1) - (2.3), (2.7) and (2.8) yield

$$I^R_{\mathbf{k}} = T^R_{\mathbf{k}}\zeta_{\mathbf{k}} + \left(T^R_{-\mathbf{k}}\zeta_{-\mathbf{k}}\right)^* \qquad (2.10)$$

We have not explicitly introduced the RAR (SAR) system transfer function into eqns (2.9) and (2.10). This may be represented simply as an additional multiplicative factor in the right-hand side of (2.10). We shall assume in the following that the system transfer function has already been incorporated in the definition of $T_{\mathbf{k}}{}^R$.

We have also ignored for simplicity the distortion effects due to the fact that a side looking radar does not, in fact, take an instantaneous snap shot but builds up an image from a sequence of consecutively imaged range strips. Thus moving waves are imaged with slightly Doppler displaced

According to standard SAR imaging theory, the azimuthal displacement ξ of the backscattering element is proportional to the range component v of the long wave orbital velocity with which the backscattering element is advected,

$$\xi = \beta v \tag{2.14}$$

where

$$\beta \;=\; (\mathit{slant\,range}\ \rho)\ /\ (\mathit{SAR\,platform\,velocity}\ U) \tag{2.15}$$

The orbital velocity v is defined here as the time average over the period during which the scattering element is viewed by the SAR. Normally, the SAR illumination time is small compared with the wave period, so that to first order v may be set equal to the instantaneous orbital velocity in the center of the viewing window.

From classical surface wave theory (Lamb, 1932),

$$v = \sum_{\mathbf{k}} T^{v}_{\mathbf{k}} \zeta_{\mathbf{k}}\, exp\,(i\,\mathbf{kr}) \quad + \quad c.c. \tag{2.16}$$

where the range velocity transfer function is given by

$$T^{v}_{\mathbf{k}} \;=\; -\,\omega\,(sin\,\theta\,\frac{k_{\ell}}{|\mathbf{k}|} \;+\; i\,cos\,\theta)\,, \tag{2.17}$$

We have neglected for simplicity the small additional Doppler shift due to the finite phase velocity of the Bragg scattering ripples. This can be readily included in the theory, but encumbers the notation. We shall also magnitude larger than the basic separation scale L_{hyd} of the standard hydrodynamic interaction and Bragg backscattering two-scale model. The scale L_{hyd} lies between the wavelength of the Bragg scattering ripples and the long waves and is thus generally of order 1 m. Since the SAR is unable to distinguish between individual backscattering facets within a SAR resolution cell, the entire ensemble of backscattering facets within a resolution cell is mapped into a single image pixel. The mean azimuthal displacement of the pixel is given by $\bar{\xi} = \beta\bar{v}$, where $\bar{v}$ is the mean orbital velocity of the cell facet ensemble. The deviations $\xi - \bar{\xi}$ of the individual facet displacements relative to this mean value then produce a smearing of the image of the resolution cell.

In Monte Carlo simulations, this sub-resolution smearing can be treated as a statistical process which can be represented simply as an effective degredation of the SAR system MTF. The long wave spectrum can then be subdivided at the scale L_{SAR}, and only waves with scales greater than L_{SAR} need be included explicitly in the simulation. The mapping computations can therefore be carried out at the relatively coarse resolution of the SAR rather than at the much finer resolution scale L_{hyd} of the backscattering facets.

In the present analysis, however, the subdivision of the wave spectrum at the SAR separation scale L_{SAR} is unnecessary, since the theory can be carried through uniformly up to the high wavenumber cut-off $(L_{hyd})^{-1}$ of the backscattering-hydrodynamic two-scale model. We may therefore regard the SAR image directly as the superposition of the (statistically independent) images of all sub-resolution scale backscattering facets, without clustering these elements together to larger entities of the dimension of the SAR resolution cell.

$$\left| \frac{\partial \xi'}{\partial r'} \right| \ll 1 \tag{2.22}$$

equ. (2.21) can be expanded in a power series and truncated after the linear term. Equs (2.20), (2.21) yield then for the SAR image amplitude spectrum, applying (2.14), (2.16),

$$I^S_{\mathbf{k}} = I^R_{\mathbf{k}} + \left(T^{vb}_{\mathbf{k}} \zeta_{\mathbf{k}} + \left(T^{vb}_{-\mathbf{k}} \zeta_{-\mathbf{k}} \right)^* \right) \tag{2.23}$$

where the velocity bunching modulation transfer function

$$\begin{aligned} T^{vb}_{\mathbf{k}} &= -i\beta k_x T^v_{\mathbf{k}} \\ &= -\beta k_x \omega \left(cos\theta - i\, sin\theta \cdot k_\ell / k \right) \end{aligned} \tag{2.24}$$

Thus in the linear approximation

$$I^S_{\mathbf{k}} = T^S_{\mathbf{k}} \zeta_{\mathbf{k}} + \left(T^S_{-\mathbf{k}} \zeta_{-\mathbf{k}} \right)^* \tag{2.25}$$

and the image variance spectrum is given by

$$P^S_{\mathbf{k}} = \left| T^S_{\mathbf{k}} \right|^2 \frac{F_{\mathbf{k}}}{2} + \left| T^S_{-\mathbf{k}} \right|^2 \frac{F_{-\mathbf{k}}}{2} \tag{2.26}$$

with the net SAR imaging modulation transfer function

$$T^S_{\mathbf{k}} = T^R_{\mathbf{k}} + T^{vb}_{\mathbf{k}} \tag{2.27}$$

3. The general nonlinear mapping relation

To determine the dependence of the SAR image Fourier components $I_{\mathbf{k}}^{S}$ on the wave Fourier components in the general nonlinear case we first apply a Fourier transform to the basic mapping relation (2.20),

$$
\begin{aligned}
I_{\mathbf{k}}^{S} &= \frac{1}{A} \int d\mathbf{r}\; exp\,(-i\mathbf{k}\cdot\mathbf{r}) \left\{ \hat{I}^{R}(\mathbf{r}') \left| \frac{d\mathbf{r}'}{d\mathbf{r}} \right| \right\}_{\mathbf{r}' = \mathbf{r} - \xi(\mathbf{r}')} \\
&= \frac{1}{A} \int d\mathbf{r}' \hat{I}^{R}(\mathbf{r}')\, exp \left[-i\mathbf{k} \cdot \left(\mathbf{r}' + \xi(\mathbf{r}') \right) \right]
\end{aligned}
\tag{3.1}
$$

Here A denotes the finite rectangular area of the sea surface corresponding to the discrete Fourier representation (in the final expression, $A \rightarrow \infty$).

Substituting the Fourier representation (2.7), (2.10) for I^{R} into (3.1), we obtain

$$
I_{\mathbf{k}}^{S} = \frac{1}{A} \int d\mathbf{r}' \left\{ 1 + \sum_{\mathbf{k}'} \left(T_{\mathbf{k}'}^{R}\, \zeta_{\mathbf{k}'} + T_{-\mathbf{k}'}^{R^{*}}\, \zeta_{-k}^{*} \right) exp\; i\mathbf{k}'\cdot\mathbf{r}' \right\} \left\{ exp \left[-i\mathbf{k}\cdot\mathbf{r}' - i\mathbf{k}\cdot\xi(\mathbf{r}') \right] \right\}
\tag{3.2}
$$

This yields for the SAR image variance spectrum

$$
\begin{aligned}
P_{\mathbf{k}}^{S} = \; &< I_{\mathbf{k}}^{S} \cdot (I_{\mathbf{k}}^{S})^{*} > \; = \; < A^{-2} \int\!\!\int d\mathbf{r}'\, d\mathbf{r}'' \left[exp \left\{ -i\mathbf{k}\cdot(\mathbf{r}' - \mathbf{r}'') - i\mathbf{k}\cdot \left(\xi(\mathbf{r}') - \xi(\mathbf{r}'') \right) \right\} \right] \cdot \\
&\left\{ 1 + \sum_{\mathbf{k}'} \left(T_{\mathbf{k}'}^{R}\, \zeta_{\mathbf{k}'} + T_{-\mathbf{k}'}^{R^{*}}\, \zeta_{-\mathbf{k}'}^{*} \right) e^{i\mathbf{k}'\cdot\mathbf{r}'} \right\} \left\{ 1 + \sum_{\mathbf{k}''} \left(T_{\mathbf{k}''}^{R^{*}}\, \zeta_{\mathbf{k}''}^{*} + T_{-\mathbf{k}''}^{R}\, \zeta_{-\mathbf{k}''} \right) e^{-i\mathbf{k}''\cdot\mathbf{r}''} \right\} >
\end{aligned}
\tag{3.3}
$$

The nonlinearity of this integral expression appears solely in the factor where

$$K_{\mathbf{k}'''} = \beta\, T^{\upsilon}_{\mathbf{k}'''}\left(e^{i\mathbf{k}'''\cdot\mathbf{r}'} - e^{i\mathbf{k}'''\cdot\mathbf{r}''}\right) \tag{3.10}$$

(cf. equ. (2.14), (2.16)). Splitting off from the sum (3.9) the sub-set S of infinitesimal wave components which appear in the products (3.5) - (3.7), and denoting the residual sum Σ' by R, we have

$$\begin{aligned}\Delta\xi &= \left(K^{*}_{\mathbf{k}'}\zeta^{*}_{\mathbf{k}'} + K^{*}_{\mathbf{k}''}\zeta^{*}_{\mathbf{k}'} + K_{-\mathbf{k}'}\,\zeta_{-\mathbf{k}'} + K_{-\mathbf{k}''}\,\zeta_{-\mathbf{k}''} + c.c\right) + \sum_{\mathbf{k}'''}{}' \left(K_{\mathbf{k}'''}\zeta_{\mathbf{k}'''} + c.c\right) \\ &= S + R\end{aligned} \tag{3.11}$$

Since S is infinitesimal, we may expand $N_{\mathbf{k}} = exp\,(\text{-}ik_x\Delta\xi)$ in a Taylor series

$$N_{\mathbf{k}} = e^{-ik_xR}\left(1 - ik_xS - k_x^2\,\frac{S^2}{2} + \dots\right) \tag{3.12}$$

The rest sum R contains only wave components which are statistically independent of the wave component factors X appearing in (3.5) - (3.7). Thus the expectation values in these expressions may be factorized in the form

$$<N_{\mathbf{k}}\cdot X> \; = \; <e^{-ik_xR}>\left(1 - ik_x <SX> - k_x^2\,\frac{<S^2X>}{2}\right) \tag{3.13}$$

The term $<SX>$ in equ. (3.13) is proportional to the wave spectrum, while the term $<S^2X>$ represents a quadratic wave spectral product. Since X is either linear (equ. (3.5)) or quadratic (equs (3.6), (3.7)), only the first two terms in the expansion (3.12) contribute to (3.13). (In the general theory is the mean square azimuthal displacement of a scattering element. We have introduced at this point the continuous spectral notation

$$F(\mathbf{k}) = \frac{F_{\mathbf{k}}}{\Delta \mathbf{k}} = \left(2\pi\right)^{-2} A \cdot F_{\mathbf{k}} \tag{3.18}$$

After some straightforward algebra to evaluate the mean products in the second parenthesis in (3.13), equ. (3.3) yields, together with (3.15) - (3.17), the closed nonlinear spectral transform expression

$$\begin{aligned} P^{s}(\mathbf{k}) = {} & (2\pi)^{-2} exp\left[-k_x^2 \, \dot{\xi}^2\right] \int d\mathbf{r}\, e^{-i\mathbf{k}\cdot\mathbf{r}} \; exp\left[k_x^2 \, \dot{\xi}^2 <v^2>^{-1} f^{v}(\mathbf{r})\right] \\ & \times \left\{1 + f^{R}(\mathbf{r}) + i k_x \beta \left[f^{Rv}(\mathbf{r}) - f^{Rv}(-\mathbf{r})\right]\right. \\ & \left. + (k_x \beta)^2 \left[f^{Rv}(\mathbf{r}) - f^{Rv}(o)\right] \left[f^{Rv}(-\mathbf{r}) - f^{Rv}(o)\right]\right\} \end{aligned} \tag{3.19}$$

where $P^{s}(\mathbf{k}) = P_{\mathbf{k}}{}^{S} / \Delta \mathbf{k}$ and

$$\begin{aligned} f^{R}(\mathbf{r}) & = <I^{R}(\mathbf{x}+\mathbf{r}) \; I^{R}(\mathbf{x})> = \\ & = \frac{1}{2} \int \left\{F(\mathbf{k}) \left| T_{\mathbf{k}}^{R} \right|^{2} + F(-\mathbf{k}) \left| T_{-\mathbf{k}}^{R} \right|^{2} \right\} e^{i\mathbf{k}\cdot\mathbf{r}} \, d\mathbf{k} \end{aligned} \tag{3.20}$$

$$\begin{aligned} f^{Rv}(\mathbf{r}) & = <I^{R}(\mathbf{x}+\mathbf{r}) \; v(\mathbf{x})> = \\ & = \frac{1}{2} \int \left\{F(\mathbf{k}) \, T_{\mathbf{k}}^{R} \left(T_{\mathbf{k}}^{v}\right)^{*} + F(-\mathbf{k}) \left(T_{-\mathbf{k}}^{R}\right)^{*} T^{v}_{-\mathbf{k}}\right\} e^{i\mathbf{k}\cdot\mathbf{r}} \, d\mathbf{r} \end{aligned} \tag{3.21}$$

$$P^{S}_{n,\,2n-2} = \Omega_n \left\{ \frac{1}{(n-1)!} f^{R}(\mathbf{r}) f^{v}(\mathbf{r})^{n-1} + \right. \tag{3.26}$$

$$\frac{1}{(n-2)!} \left[f^{Rv}(\mathbf{r}) - f^{Rv}(0) \right] \left[f^{Rv}(-\mathbf{r}) - f^{Rv}(0) \right] f^{r}(\mathbf{r})^{n-2}$$

where Ω_n is the Fourier transform operator

$$\Omega_n = (2\pi)^{-2} \int d\mathbf{r}\, exp\,(-i\,\mathbf{k}\cdot\mathbf{r}) \tag{3.27}$$

(for the integers 0, -1 the factorial function is defined as $0! = 1$ and $((-1)!)^{-1} = 0$).

We have left out a term $P_{0,0}$ in the sum representing an irrelevant δ-function contribution at $\mathbf{k} = 0$ associated with the mean image intensity.

An expansion with respect to nonlinearity only can be obtained by summing over the velocity bunching index m for fixed nonlinearity order n,

$$P^{S}(\mathbf{k}) = exp\left(-k_x^2\, \xi'^2\right) \left(P_1^S(\mathbf{k}) + P_2^S(\mathbf{k}) + \ldots P_n^S(\mathbf{k}) + \ldots\right) \tag{3.28}$$

The linear term $P_1{}^S$ is found to be identical (as it must be) with the linear SAR spectrum of equ. (2.26).

It should be noted that the terms $P_n{}^S(\mathbf{k})$ in equ. (3.28) do not represent the direct expansion of $P^S(\mathbf{k})$ in powers of the input wave spectrum, as the common (nonlinear) azimuthal cut-off factor $exp\,(-k_x{}^2\,\xi'^2)$ has been taken out of the sum. This is an important feature of the theory.

where the pure RAR spectrum $P^R_{q\ell}$, the pure quasi-linear velocity bunching spectrum $P_{q\ell}^{vb}$ and the quasi-linear interference spectral term $P_{q\ell}^{int}$ are given by

$$\left\{ \begin{matrix} P^R_{q\ell} \\ \\ P^{int}_{q\ell} \\ \\ P^{vb}_{q\ell} \end{matrix} \right\} = exp\left(-k_x^2 \, \xi'^2 \right) \left\{ \begin{matrix} P^S_{10} \\ \\ (k_x \beta) P^S_{11} \\ \\ (k_x \beta)^2 \, P^S_{12} \end{matrix} \right\} \qquad (3.31)$$

Applying eqns (2.26), (2.27) this may be written

$$P^{\cdot\cdot}_{q\ell} = H^{\cdot\cdot}_{\mathbf{k}} \frac{F_k}{2} + H^{\cdot\cdot}_{-\mathbf{k}} \frac{F_{-k}}{2} \qquad (\mathit{for\,any\,index}\ ..\ R,\, int,\, vb \ \mathit{or}\ S) \qquad (3.32)$$

where

$$\left\{ \begin{matrix} H^R_{\mathbf{k}} \\ \\ H^{int}_{\mathbf{k}} \\ \\ H^{vb}_{\mathbf{k}} \\ \\ H^S_{\mathbf{k}} \end{matrix} \right\} = exp\left(-k_x \, \xi'^2 \right) \left\{ \begin{matrix} \left| T^R_{\mathbf{k}} \right|^2 \\ \\ \left(T^R_{\mathbf{k}} \cdot T^{vb^*}_{\mathbf{k}} + T^{R^*}_{\mathbf{k}} \, T^{vb}_{\mathbf{k}} \right) \\ \\ \left| T^{vb}_{\mathbf{k}} \right|^2 \\ \\ \left| T^S_{\mathbf{k}} \right|^2 \end{matrix} \right\} \qquad (3.33)$$

The orientations in the complex plane of the various MTF's which determine the filter factors $H_{\mathbf{k}}^{\cdot\cdot}$ are indicated in Fig. 1. The MTF's apply for a given surface wave component and various sign combinations of the SAR look and flight directions. Panel a applies to a wave component travelling in the positive quadrant of the xy-plane $(k_x > 0\,,\,k_y > 0)$ and a left looking SAR $(k_\ell = k_y)$. Panel b applies for the same left-looking SAR viewing the same wave component but for a SAR platform flying in the opposite direction ($k_x < 0$, $k_y = k_\ell < 0$). Panels c, d correspond to panels a, b respectively, for a right-looking SAR ($k_\ell = -k_y$). The resultant SAR MTF is seen to be strongly dependent on the orientation of the SAR look and flight directions. This has been confirmed by aircraft SAR measurements (e.g. Hasselmann et al., 1990).

The strong dependence on the viewing geometry is at first sight perhaps surprising, since the moduli of the individual velocity bunching, tilt and hydrodynamic transfer functions are invariant with respect to the four viewing combinations shown in Fig. 1. The modulus of the net RAR transfer function is also only weakly dependent on the look and flight direction (through the imaginary component of the hydrodynamic MTF, which, in contrast to the imaginary tilt MTF, is invariant with respect to the look and flight direction).

Since the moduli of the separate filter functions $H_{\mathbf{k}}^R$ and $H_{\mathbf{k}}^{vb}$ for pure RAR and pure velocity bunching imaging, respectively, are approximately or exactly independent of the sign combinations of the viewing geometry, the strong viewing geometry dependence of the net SAR filter function

$$H_{\mathbf{k}}^S = H_{\mathbf{k}}^\ell + H_{\mathbf{k}}^{int} + H_{\mathbf{k}}^{vb} \tag{3.34}$$

must come about through the interference filter function $H_{\mathbf{k}}^{int}$.

This is illustrated by the plots of the four filter functions $H_{\mathbf{k}}^R$, $H_{\mathbf{k}}^{int}$, $H_{\mathbf{k}}^{vb}$ and $H_{\mathbf{k}}^S$ shown in Fig. 2. The cut-off scale was chosen as $\xi' = 70$ m, or $k_x^{cut\,off} = (\xi')^{-1} = 0.014$ m^{-1}, corresponding to the SEASAT value $\beta = 113.5$ and a Pierson-Moskowitz (1964) fully developed wind sea spectrum for a wind speed at 10 m height of 10 m/s ($<v^2>^{1/2} = 0.62$ m/s). The damping factor in $T_{\mathbf{k}}^{hyd}$ (equ. (2.6)) was set at $\mu = 0.5\,sec^{-1}$ and no wind input modulation terms were included (as in the SEASAT computations in Section 5).

The filter function $H_{\mathbf{k}}^{vb}$ is seen to be exactly symmetrical with respect to a change in sign of k_x or k_y, the filter function $H_{\mathbf{k}}^{R}$ is exactly symmetrical with respect to a change in sign of k_x and approximately symmetrical with respect to a change in sign of k_y, while the filter function $H_{\mathbf{k}}^{int}$ is exactly anti-symmetrical with respect to the transformation $k_y \rightarrow -k_y$. The net filter function $H_{\mathbf{k}}^{S}$ is therefore approximately symmetrical with respect to a change in sign of k_y, but has pronounced asymmetries with respect to the transformation $k_x \rightarrow -k_x$.

The general structures of the filter functions shown in Fig. 2 are independent of the parameters chosen. It will be useful to keep Fig. 2 in mind later in discussing the origin of the various distortions and asymmetries found in computed and observed SAR image spectra.

As pointed out, the common azimuthal cut-off factor applies not only to the quasi-linear spectral terms but also to the entire series expansion (3.23) or (3.28). This has a useful practical implication. The azimuthal cut-off of an observed SAR spectrum is usually a relatively well-defined feature. Its experimental determination, independent of the details of the mapping process, yields an important integral property of the wave spectrum, the mean square orbital velocity (cf. equ. (3.17)).

Beal et al. (1983), Lyzenga (1986) and Monaldo and Lyzenga (1986, 1988) have verified experimentally the proportionality of the azimuthal cut-off scale to the rms orbital range velocity component - or some related integral property of the wave field. Previously, this finding has been difficult (power of βk_x) can be collected together and Fourier transformed in a single operation.

Since only Fourier transforms are involved, the computations are rather fast (less than 1 sec on a CRAY-2, but efficient computation can presumably be achieved also with PCs using hard wired FFTs.) Good convergence was normally attained even for strongly nonlinear spectra with a truncation at nonlinearity order $n = 6$. The higher order terms contribute mainly to the resolution of the (normally not very important) details near the azimuthal cut-off (cf. Sections 5, 6).

matrix for the combined data set $\hat{P}(\mathbf{k})$, $\hat{F}(\mathbf{k})$ – cannot be readily estimated in our case, these options were not further pursued.

However, to enhance the agreement of the computed and observed SAR spectra in the neighbourhood of the SAR spectral peaks, we considered also the alternative cost function

$$J' = \int \left[P(\mathbf{k}) - \hat{P}(\mathbf{k})\right]^2 \cdot \hat{P}(\mathbf{k})\, d\mathbf{k} + \mu \int \left\{ \frac{[F(\mathbf{k}) - \hat{F}(\mathbf{k})]}{[B + \hat{F}(\mathbf{k})]} \right\}^2 d\mathbf{k} \tag{4.2}$$

with an additional factor $\hat{P}(\mathbf{k})$ in the first integral.

The solution of the general nonlinear variational problem

$$\frac{\delta J}{\delta F(\mathbf{k})} = 0 \tag{4.3}$$

was obtained by an iterative technique which made use of the approximate quasi-linear mapping relation (3.29), as follows:

Starting from a first estimate $F^1(\mathbf{k}) = \hat{F}(\mathbf{k})$, let $F^n(\mathbf{k})$, $P^n(\mathbf{k})$ represent the approximate solution after n iteration steps, where $P^n(\mathbf{k})$ is the associated SAR spectrum for the wave spectrum $F^n(\mathbf{k})$ in accordance with the fully nonlinear mapping relation (3.28),

$$P^n = M_{n\ell}(F^n) \tag{4.4}$$

Construct now an improved solution

$$F^{n+1} = F^n + \Delta F^n \tag{4.5}$$

$$B_{\mathbf{k}} = W_{\mathbf{k}} W_{-\mathbf{k}} \tag{4.13}$$

and

$$W_{\mathbf{k}} = \left| T^S(\mathbf{k}) \right|^2 exp\left(-k_x^2 \xi'^2 \right) \tag{4.14}$$

Having determined ΔF^n and the new wave spectrum F^{n+1}, the iteration step is then completed by computing the associated SAR spectrum, using the fully nonlinear transformation relation $P^{n+1} = M_{n\ell}(F^{n+1})$.

The technique can be applied equally well to the form (4.2). In computing the perturbations $\Delta F^n, \Delta P^n$, the additional factor P in the first integral in J is set equal in this case to P^n.

The iteration scheme was found to converge in all cases studied, including cases with strongly nonlinear and poor first guesses, provided μ was not chosen too small, namely $\mu \gtrsim \mu_0$, where

$$\mu_0 = 0.1 \cdot \hat{P}^2_{max} \tag{4.15}$$

In most applications we chose $\mu = \mu_0$. The constant B was set at $0.01 \cdot \hat{F}_{max}$.

In the SEASAT cases discussed in the following section, the SAR calibration was not known. This can be readily accommodated in the inversion formalism by including the dependency on the unknown calibration factor explicitly in the expression for J and minimizing the cost function simultaneously with respect to both F and the unknown calibration factor. The minimization with respect to the calibration factor can be given analytically and was carried out after each iteration step.

coupling to the wind field, some form of dynamical constraints are needed. These were introduced using the following simple two-stage procedure:

As the high wavenumber region of the spectra is strongly coupled to lower wavenumbers through the nonlinear transfer, we restricted the modification of the spectrum in the first inversion stage to transformations which apply uniformly to the entire wave spectrum. The simplest such transformation is a rotation ϕ_0 in the wavenumber plane combined with scale changes A, B in the energy and wavenumber, respectively,

$$F'(\mathbf{k}) = A\, F(\mathbf{k}') \tag{4.16}$$

where

$$\begin{aligned} k_x' &= B\,(k_x \cos\phi_0 - k_y \sin\phi_0) \\ k_y' &= B\,(k_x \sin\phi_0 + k_y \cos\phi_0) \end{aligned} \tag{4.17}$$

After minimizing the cost function with respect to the parameters ϕ_0, A, B, the original minimization procedure without constraints was then applied in a second stage.

The first stage normally yielded a close fit to the SAR spectral peak, while ensuring continuity of the overall spectral distribution. The second stage then provided further fine scale adjustments within the azimuthal wavenumber band for which detailed SAR information was available. Since a reasonable first order fit was achieved already in the first stage, the second stage no longer produced significant dislocations in the azimuthal cut-off region.

5. Some examples from SEASAT

The computation of the forward transformation relation is illustrated in Fig. 3 for a typical SEASAT case. The case was selected together with the two other cases discussed in this section from a larger set of SAR image spectra analyzed in the course of a wave hindcast study using the WAM third generation wave model (WAMDIG, 1988; Hasselmann et al., 1988).

The individual panels show the hindcast WAM wave spectrum, the SAR spectrum computed from the WAM spectrum, and some typical spectral terms of the nonlinear spectral expansion. The case is only weakly nonlinear, so that only little of the azimuthally travelling short wave energy is lost in the SAR image, while most of the wave energy propagating in the range direction is retained. The quasi-linear approximation, consisting of the sum of the first three quasi-linear contributions is seen to yield a fairly good approximation of the fully nonlinear image.

The splitting of the single wave spectral peak into two peaks in the SAR image spectrum is a common feature in SAR images of predominantly range travelling waves. It arises because the velocity bunching MTF, which normally dominates over the RAR MTF, vanishes in the range direction (cf. Section 3 and Fig. 2).

The asymmetry of the SAR response about the look direction due to the interference term (cf. Fig. 2) is evident in the interference term and in the resulting quasi-linear and fully nonlinear SAR spectra. In general, all terms with odd powers of $(k_x \beta)$ contribute to the asymmetry. As pointed out in Section 3, the asymmetry is dependent on the look and flight directions, so that different SAR image spectra are obtained, for example, if the same wave field is viewed from the upwind or downwind direction (Hasselmann et al., 1990). In comparing Figs 2 and 3 it should be noted that the SAR spectrum is formed from both positive and negative $\mathbf{k}$ contributions (cf. eqn. (2.26)). Thus in contrast to the filter functions of Fig. 2, which apply for only one wave component, the spectra of Fig. 3 are symmetrical with respect to the transformation $\mathbf{k} \rightarrow -\mathbf{k}$.

The higher order terms in the expansion are proportional to the product of a high power of $(k_x \beta)$ with the exponential azimuthal cut-off factor and are therefore normally strongly peaked along the azimuthal cut-off band. These terms do not contribute significantly to the structure of the SAR spectrum in the neighbourhood of the spectral peak, so that the effective convergence of the series in the main part of the spectrum is rather rapid (see also Fig. 5, discussed below).

Fig. 4 shows a comparison of the observed SAR spectra and the computed wave and SAR spectra before and after inversion for the three SEASAT cases. Through the combined effects of the azimuthal cut-off, the strongly varying modulation transfer functions (cf. Fig. 2) and the nonlinear distortions, the observed and computed SAR spectra (first and third columns, respectively) show relatively little similarity with the hindcast first guess wave spectra (second column). The first guess SAR spectra computed from the hindcast wave spectra reproduce the azimuthally banded structure of the observed SAR spectra, but none the less still show significant deviations.

The fourth and fifth columns show the best fit wave spectra and the associated computed SAR spectra derived by the inversion method. The agreement between the best fit and observed SAR spectra is now seen to be markedly improved. The parameters of the hydrodynamic MTF (equ. 2.6) were chosen in all cases as $\mu = 0.5 \text{ sec}^{-1}$ and $\gamma = 0$. This is consistent with field and laboratory measurements (cf. Keller and Wright, 1975; Plant et al., 1983; Feindt et al., 1986; Schröter et al., 1986), but no attempt was made to optimize these parameters. The inversions were based on the peak-enhanced cost function (4.3).

The three cases were selected to illustrate different degrees of nonlinearity and different directions of wave propagation relative to the SAR look direction. The first case is weakly nonlinear, with predominately range propagating waves. The second case is moderately nonlinear and represents a wave field propagating at an angle between the range and azimuthal directions. The third case, finally, is strongly nonlinear and was chosen also as an example of a more complex sea state, consisting of a superposition of swell and windsea components propagating at nearly 90° relative to one another. The azimuthally propagating major swell component is seen to almost entirely lost due to the azimuthal cut-off.

The individual modifications introduced into the best fit wave spectra through the two step inversion procedure (summarized in Table 1) can be clearly recognized:

(i) The spectra have been rotated and the wavenumber scales adjusted to reproduce the positions of the SAR spectral peaks.

(ii) The energy scales have been adjusted (together with the wavenumber scales) to reproduce the observed azimuthal cut-offs. This effect is evident in the changed azimuthal limits between the first guess and best fit SAR spectra (columns 3 and 5).

stage inversion procedure will be ultimately superceded by a comprehensive data assimilation scheme in which the measured SAR spectrum is used to modify the wind field rather than the wave spectrum directly.

The convergence properties of the spectral expansion (3.23) for the three cases considered are indicated in Fig. 5. Terms of different nonlinearity order n for a given velocity bunching order m (which appear in the same Fourier transform contribution) have been collected into a single term. The curves show the maximal spectral values for each m'th order spectrum of the expansion. Since these values, as already mentioned, tend to lie near the relatively unimportant azimuthal cut-off limits for the higher order expansion terms, the effective convergence is in fact better than implied by the figure. In practice, good convergence was achieved in all cases studied with a truncation of the series, at $m = 12$ ($n = 6,7$).

6. Some examples from LEWEX

As further illustration we apply the transform relation to two cases from the Labrador Extreme Waves Experiment (cf. Hasselmann et al., 1990). The input wave spectra for the transformation computations were taken from the observed directional wave buoy (Wavescan) data and from a wave hindcast using the WAM third generation wave model (WAMDIG, 1988). A comparison of the hindcast wave fields with wave buoy observations indicated that the hindcast was acceptable as a first guess, although some systematic deviations were found (cf. Fig. 6). The cases were selected from larger data sets which were analysed as part of a more extensive wave hindcast study (Brüning and Zambresky, in preparation).

The principal SAR parameters of the two runs are listed in Table 2. The polarization was HH and the look direction to the right for both runs. The damping factor μ and wind input modulation term γ in the hydrodynamic MTF were set equal to zero. The images for both runs were taken over essentially the same wave field, but the two SAR flight directions were opposite and the aircraft altitude and thus the β parameters (ρ/U) differed by a factor of nearly two.

Figs 6 and 7 show a comparison of the observed and computed SAR spectra for the two cases. The two rows in each figure correspond to different input wave spectra, shown in the left column. Also shown are the Monte Carlo computations (kindly provided by C. Brüning) for the case of the wave scan spectra (bottom right).

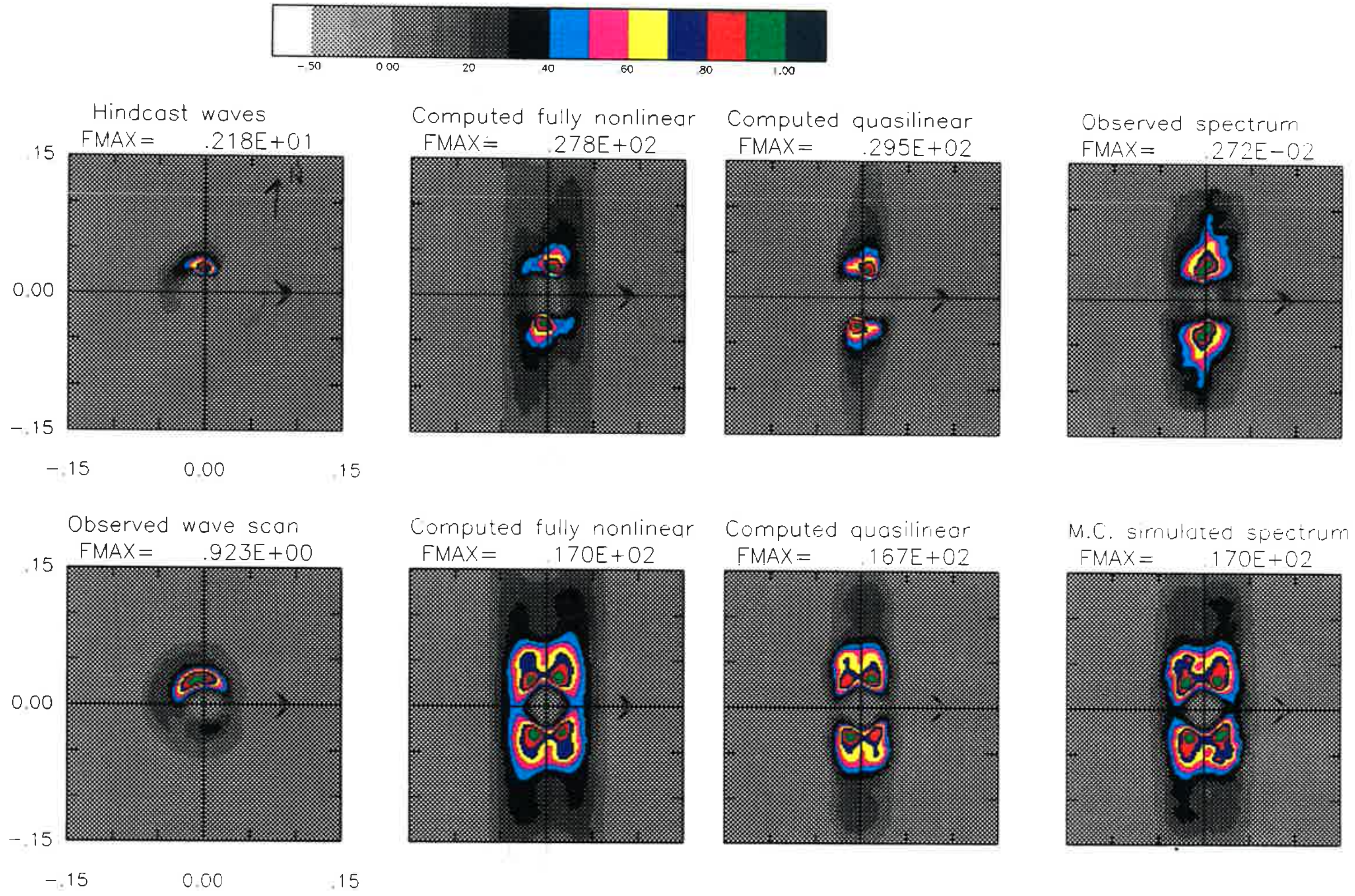

Fig. 6 Hindcast (top row) and observed (wave scan, bottom row) wave spectra together with computed SAR spectra for LEWEX case 1. The observed SAR spectrum is shown in the top right panel. The bottom right panel shows the Monte Carlo simulated SAR spectrum for the wave scan wave spectrum. The aircraft flight direction is in the x-direction.

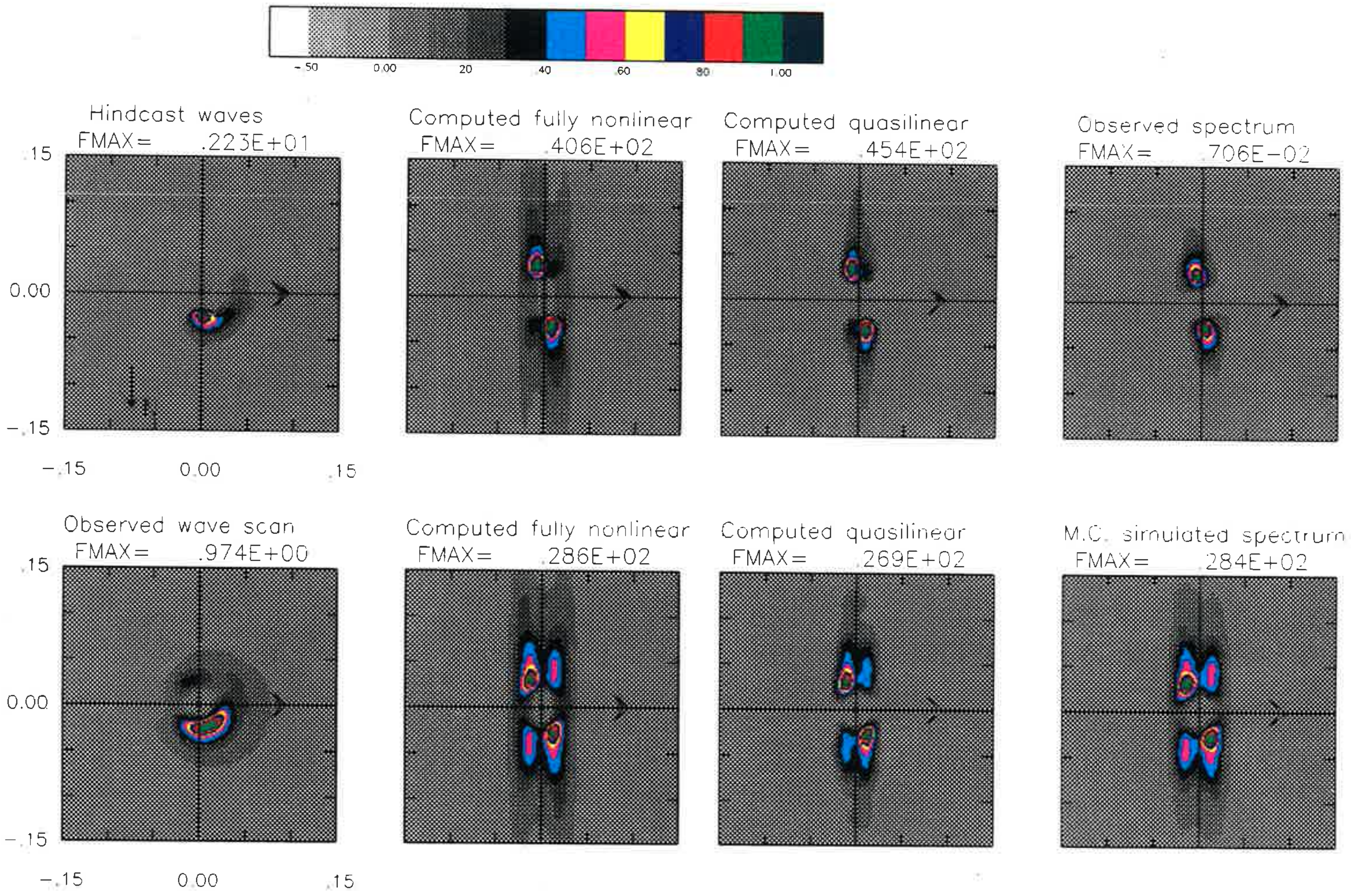

Fig. 7 Same as Fig. 6 for LEWEX case 2. The aircraft flight direction is opposite to that of case 1. Coordinates are defined as before in the aircraft frame.

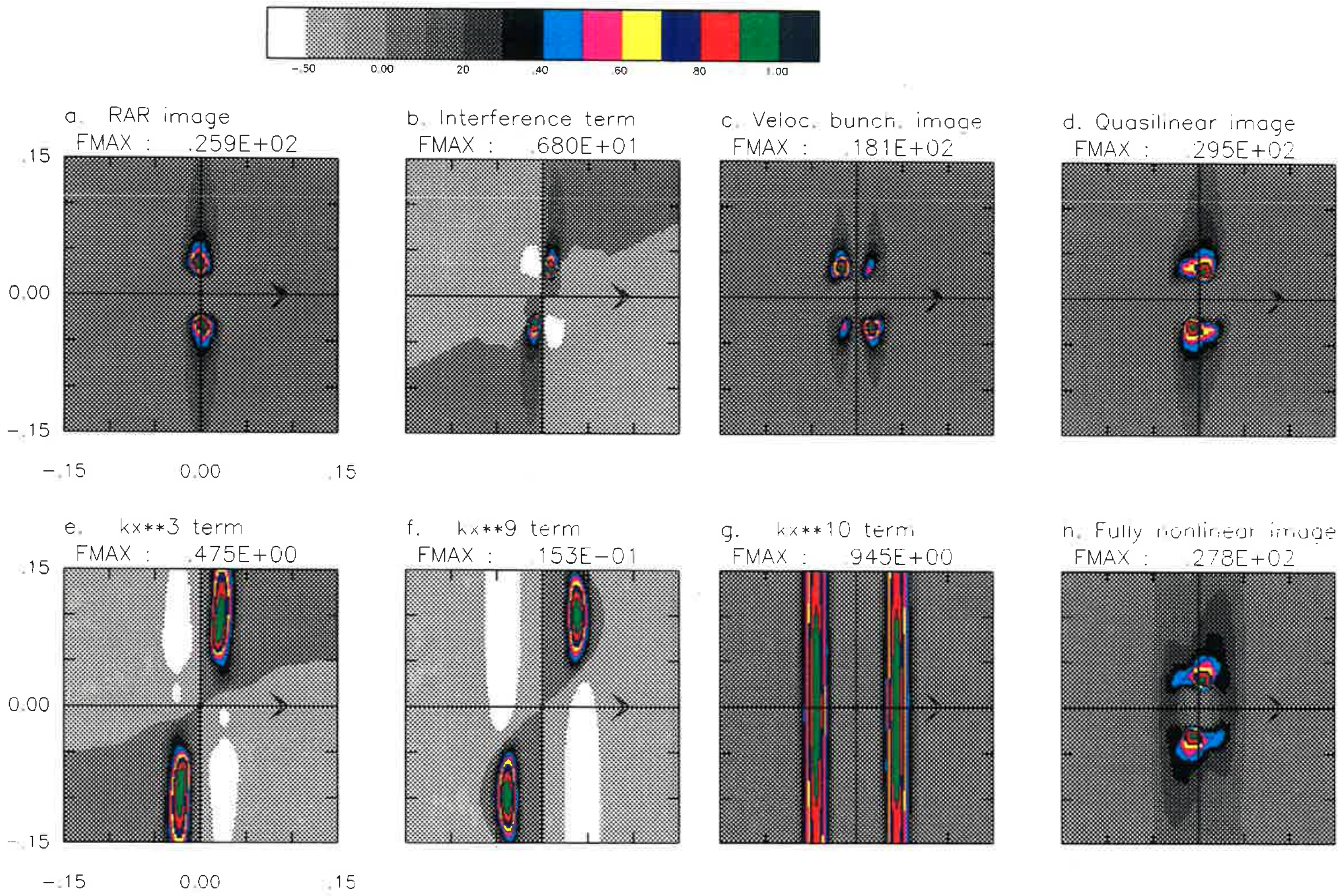

Fig. 8 Contributions of various spectral expansion terms to the SAR spectral image for LEWEX case 1. Note the asymmetry about the look direction induced by the terms with odd kx powers m. The dominant asymmetry arises from the linear RAR-velocity bunching interference term (m = 1, n = 1).

Several features are apparent:

(1) As in the SEASAT cases, the SAR wave image spectra show rather little resemblance to the (symmetrized) input wave spectra. This is, of course, a well-known feature of SAR spectra. However, it has perhaps not always been fully appreciated that the distortion can be pronounced not only for azimuthally travelling waves, for which the nonlinearities are large, but also for relatively linear range travelling waves, as in these cases.

(2) The azimuthal cut-off is well defined and occurs at a lower wavenumber for the higher altitude flight, as expected.

(3) The SAR spectra show evidence of some azimuthal asymmetry relative to the SAR look direction which is not apparent in the original wave spectra. The asymmetry depends on the wave propagation direction relative to the SAR look direction: in case 1 (Fig. 6), waves in the top right quadrant are enhanced relative to the waves in the top left quadrant, whereas in case 2 (Fig. 7) waves in the bottom right quadrant (corresponding to the top left quadrant in the 180° rotated spectrum of Fig. 6) are enhanced relative to the bottom left quadrant. The fact that the asymmetry depends on the SAR look direction – both in the simulations and the observations – is a clear indication that it represents an artifact of the imaging and not a real feature of the wave spectrum.

(4) The theoretical SAR spectra agree reasonably well with the measured SAR spectra in all cases. This, together with the features listed above, underlines again the need for a first guess input wave spectrum and

The interference between the frozen surface and velocity bunching modulation can be identified explicitly in the expansion (3.23). The relevant spectral distributions are shown in Fig. 8 for case 1. The first term $C \cdot P^S_{10}$ $(n = 1, m = 0)$ (panel a) represents the frozen surface contribution (but with the inclusion of the azimuthal cut-off factor). It is positive everywhere and reproduces the approximately symmetrical distribution of the wave spectrum about the SAR look direction. The second term $C \cdot (k_x \beta) P^S_{11}$ $(n = 1, m = 1)$ (panel b) represents the quadratic interference between the frozen surface and velocity bunching transfer functions. It is asymmetrical, alternating in sign between quadrants. The third term $C \cdot (k_x \beta)^2 P^S_{12}$ $(n = 1, m = 2)$, panel c, represents the pure (quasi-linear) velocity bunching term, without the RAR contribution. It is again positive and symmetrical. The sum of the first three terms yields the quasi-linear SAR spectrum, equ. (3.29), panel d (which is shown also in the corresponding panel of Fig. 6). The asymmetry of the quasi-linear spectrum is seen to arise from the interference term. Asymmetries occur in general in all higher order, odd-m terms of the expansion (e.g. panels e, f), contributing to the asymmetry of the final nonlinear SAR spectrum, panel h. Panel g $(m = 10)$ shows an example of a higher order symmetrical spectral term. It exhibits a pronounced concentration along the azimuthal cut-off line which is characteristic of all higher order terms and arises from the product of the factor $(k_x \beta)^m$ with the exponential azimuthal cut-off factor.

6. Conclusions

The new closed nonlinear integral transformation relation derived in this paper, together with its expansion in a spectral series with respect to nonlinearity and velocity bunching order, presents a number of advantages:

- It can be computed rather rapidly using Fast Fourier Transforms and is free of the statistical sampling errors of Monte Carlo methods. It should thus make feasible the operational processing of SAR wave images which will be obtained from future satellites such as ERS-1, 2 and Radarsat.

- It provides a clearer insight into the imaging mechanism by identifying the different contributions from the RAR modulation and nonlinear velocity bunching processes and their various interference terms.

- It yields a simple expression for the azimuthal cut-off in the form of a Gaussian filter factor which acts on all terms in the series expansion. The azimuthal cut-off scale is given by the rms azimuthal velocity bunching displacement. The observed azimuthal cut-off therefore yields a useful integral constraint on the wave spectrum.

- The lowest order quasi-linear term of the spectral series expansion, consisting of the product of the standard linear SAR spectrum and the azimuthal cut-off factor, yields a useful first order approximation of the fully nonlinear mapping relation.

Appendix

Extension to acceleration smearing and general dispersive mapping

The pure velocity bunching theory presented in Section 3 is non-dispersive: an infinitesimal cross-section element $\sigma(\mathbf{r}')\,d\mathbf{r}'$, which in the absence of motion effects would correspond to an image element $\hat{I}^R(\mathbf{r}')\,d\mathbf{r}' = \sigma(\mathbf{r}')\,d\mathbf{r}'/\bar{\sigma}$, is mapped one-to-one into a displaced infinitesimal element

$$\hat{I}^S(\mathbf{r})\,d\mathbf{r} = \hat{I}^R(\mathbf{r}')\,d\mathbf{r}' \qquad \text{(A.1)}$$

in the SAR image plane, where

$$r = \mathbf{r}' + \xi\,(\mathbf{r}') \qquad \text{(A.2)}$$

and $\xi = \mathrm{a}\beta\upsilon$ (equ. 2.12).

In the general SAR theory of ocean wave imaging for arbitrarily moving scattering elements, the mapping is dispersive (cf. MSR): an infinitesimal element on the sea surface is mapped into a finite patch in the SAR image plane. The form (A.1) must accordingly be generalized to the integral relation

$$\hat{I}^S(\mathbf{r}) = \int \hat{I}^R(\mathbf{r}')\,M(\mathbf{r}-\mathbf{r}';\mathbf{r}')\,d\mathbf{r}' \qquad \text{(A.3)}$$

The mapping function $M(\mathbf{r}\text{-}\mathbf{r}';\mathbf{r}')$ represents a finite width distribution with respect to the primary spatial separation variable $\mathbf{r}\text{-}\mathbf{r}'$ and depends in general also on the details of the motion history of the scattering element at $\mathbf{r}'$. To a good approximation, the shape of M is given by the shape of the Doppler spectrum of the backscattered return signal (MSR).

where $H(\eta)$ denotes the top hat function

$$H(\eta) = \begin{cases} 1 & for \quad |\eta| \leq \frac{1}{2} \\ 0 & for \quad |\eta| > \frac{1}{2} \end{cases} \tag{A.7}$$

In place of (A.6) a Gaussian distribution

$$M^g(\mathbf{r}-\mathbf{r}';\mathbf{r}') = (2\pi)^{-\frac{1}{2}}(\Delta x)^{-1} exp\left\{\frac{(x-x'-\xi(\mathbf{r}'))^2}{2(\Delta x)^2}\right\}\delta(y-y') \tag{A.8}$$

with the same rms width

$$\Delta x(\mathbf{r}') = \frac{\beta\tau|a(\mathbf{r}')|}{2\sqrt{3}} \tag{A.9}$$

as the top hat form (A.6) is sometimes used (cf. Alpers and Brüning, 1986). This simplifies the treatment of acceleration smearing within the framework of a more general analysis including the effects of the antenna pattern and the matched filter and other SAR system characteristics.

The distinction between (A.6) and (A.8) is immaterial in the present context. We shall show that if the function M is known, regardless of the model used, the surface wave-SAR image spectral mapping relations can be derived as before in closed form.

Starting from the general form (A.2), the expression (3.1) for the Fourier components of the SAR image now become (for $\mathbf{k} \neq 0$, so that $I(\mathbf{r})$ may be replaced by $\hat{I}(\mathbf{r})$),

$$G_{\mathbf{k}}^{h,g} = exp\,[-i\,\mathbf{k}\cdot\xi(\mathbf{r}')]\,D^{h,g} \tag{A.15}$$

which contains an additional azimuthal acceleration smearing term

$$D^{h} = \frac{sin\,(\sqrt{3}\;k_x\,|\Delta x|)}{\sqrt{3}\;k_x\,|\Delta x|} \tag{A.16}$$

or

$$D^{g} = exp\left(\frac{-k_x^2\cdot\Delta x^2}{2}\right) \tag{A.17}$$

The further analysis proceeds as in Section 3, with the velocity bunching weighting function $exp[-i\,\mathbf{k}\cdot\xi(\mathbf{r}')]$ replaced by the general weighting function $G_{\mathbf{k}}$. The expression (3.3) for the SAR image variance spectrum becomes

$$P_{\mathbf{k}}^{S} = A^{-2} < \int\int d\mathbf{r}'\,d\mathbf{r}''\,exp\left[-i\,\mathbf{k}\,(\mathbf{r}'-\mathbf{r}'')\right]\cdot N_{\mathbf{k}}\cdot D(\mathbf{r}')\,D(\mathbf{r}'') \tag{A.18}$$
$$\left\{1 + \sum_{\mathbf{k}'}\left(T_{\mathbf{k}'}^{R}\,\zeta_{\mathbf{k}'} + T_{-\mathbf{k}'}^{R^*}\,\zeta_{-\mathbf{k}'}^{*}\right)e^{i\mathbf{k}'\cdot\mathbf{r}'}\right\}\left\{1 + \sum_{\mathbf{k}''}\left(T_{\mathbf{k}''}^{R^*}\,\zeta_{\mathbf{k}''}^{*} + T_{-\mathbf{k}''}^{R}\,\zeta_{-\mathbf{k}''}\right)e^{-i\mathbf{k}''\cdot\mathbf{r}''}\right\} >$$

The expression differs from (3.3) only through the inclusion of the acceleration smearing factors $D(\mathbf{r}')\cdot D(\mathbf{r}'')$.

To evaluate the expectation value occurring in the RHS of equ. (A.18) the same technique may be applied as before. The product $D(\mathbf{r}')\cdot D(\mathbf{r}'')$ is first expanded in a power series with respect to the wave Fourier amplitudes. For the forms (A.16) or (A.17), this is straightforward. The expectation value of the product of $N_{\mathbf{k}}$ with the various wave amplitude products occurring in the rest of

References

Alpers, W., 1983. Monte Carlo simulations for studying the relationship between ocean wave and synthetic aperture radar image spectra. Journal of Geophysical Research, **88**, 1745.

Alpers, W., and C.L. Rufenach, 1979. The effect of orbital motions on synthetic aperture radar imagery of ocean waves. IEEE Trans. Antennas Propag., **AP-27**, 685 - 690.

Alpers, W., D.B. Ross, and C.L. Rufenach, 1981. On the detectability of ocean surface waves by real and synthetic aperture radar. Journal of Geophysical Research, **86**, 6481 - 6498.

Alpers, W., and K. Hasselmann, 1982. Spectral signal-to-clutter and thermal noise properties of ocean wave imaging synthetic aperture radars. International Journal of Remote Sensing, **3**, 423 - 446.

Alpers, W., C. Brüning, and K. Richter, 1986. Comparison of simulated and measured synthetic aperture radar image spectra with boy-derived ocean wave spectra during the Shuttle Imaging Radar-B mission. IEEE Transactions on Geoscience and Remote Sensing, SIR-B special issue, GE-24, 559.

Alpers, W., and C. Brüning, 1986. On the relative importance of motion-related contributions to the SAR imaging mechanism of ocean surface waves. IEEE Transactions on Geoscience and Remote Sensing, GE-24, 873.

Hasselmann, K., T.P. Barnett, E. Bouws, H. Carlson, D.E. Cartwright, K. Enke, J.A. Ewing, H. Gienapp, D.E. Hasselmann, P. Kruseman, A. Meerburg, P. Müller, D.J. Olbers, K. Richter, W. Sell, and H. Walden, 1973. Measurements of wind-wave growth and swell decay during the Joint North Sea Wave Project (JONSWAP). Ergänzungsheft zur Deutschen Hydrographischen Zeitschrift, Reihe A(8°), No. 12.

Hasselmann, K., D.B. Ross, P. Müller, and W. Sell, 1976. A parametric wave prediction model. Journal of Physical Oceanography, **6**, 200 - 228.

Hasselmann, K., R.K. Raney, W.J. Plant, W. Alpers, R.A. Shuchman, D.R. Lyzenga, C.L. Rufenach, and M.J. Tucker, 1985. Theory of synthetic aperture radar ocean imaging: A MARSEN View. Journal of Geophysical Research, **90**, 4659 - 4686.

Hasselmann, K., S. Hasselmann, E. Bauer, C. Brüning, S. Lehner, H. Graber, P. Lionello, 1988. Development of a satellite SAR image spectra and altimeter wave height data assimilation system for ERS-1. ESA Contract Report and MPI-Report No. 19.

Hasselmann, K., S. Hasselmann, C. Brüning, and A. Speidel, 1990. Application of a new closed ocean wave-SAR spectral transform relation to LEWEX data. Measuring, Modeling, Predicting and Applying Directional Ocean Wave Spectra, The Johns Hopkins University, 18. - 20. April 1989.

Kenney, J.E., E.A. Uliana, and E.J. Walsh, 1979. The surface contour radar, a unique remote sensing instrument. IEEE Transactions on Microwave Theory and Techniques MTT 27, 1080 - 1092.

Komen, G.J., S. Hasselmann, and K. Hasselmann, 1984. On the existence of a fully developed wind-sea spectrum. Journal of Physical Oceanography, **14**, 1271 - 1285.

Lamb, H., 1932. Hydrodynamics. 6th edition, 738 pp., Dover.

Lyzenga, D.R., 1986. Numerical simulation of synthetic aperture radar image spectra for ocean waves. IEEE Transactions on Geoscience and Remote Sensing, GE-24, 6, 863.

Monaldo, F. M., and D. R. Lyzenga, 1986. On the estimation of slope- and height-variance spectra from SAR imagery, IEEE Transactions on Geoscience and Remote Sensing, GE-24, 543-551.

Monaldo, F. M., and D. R. Lyzenga, 1988. Comparison of Shuttle Imaging Radar-B ocean wave spectra with linear model predictions based on aircraft measurements, Journal of Geophysical Research, **93**, 15, 374 - 388.

Pierson, W.J., Jr., and L. Moskowitz, 1964. A proposed spectral form for fully developed wind seas based on the similarity theory of S.A. Kitaigorodskii. Journal of Geophysical Research, **69**, 5181.

Plant, W.J., 1987. The microwave measurement of ocean-wave directional spectra. Johns Hopkins APL Technical Digest. Volume 8, No. 1, 55.

Walsh, E.J., D.W. Hancock III, D.E. Hines, R.N. Swift, and J.F. Scott, 1990. Evolution of the directional wave spectrum from shoreline to fully developed. Journal of Physical Oceanography (in press).

WAMDIG, 1988. The WAM model - a third generation ocean wave predition model. Journal of Physical Oceanography, **18**, 1775 - 1810.

Wright, J.W., 1968. A new model for sea clutter, 1968. IEEE Trans. Antennas Propag., **AP-16**, 217 - 223.

Part 2

Study of the impact of the surface wave field on the C-band model function and the derived wind vector.

by

Knut Barthel
Klaus Hasselmann

where k_b is the wavenumber of the Bragg resonant wave

$$k_b = -2 \sin\theta \ k_e \tag{6}$$

and a and S are the Phillips constant and the short wave spread function given by,

$$a = a_0 + a_1 \left(U \sqrt{\frac{|k_b|}{g}}\right)^n \tag{7}$$

$$S = N \left[\cos^{2p}\left(\frac{\phi}{2}\right) + \sin^{2p}\left(\frac{\phi}{2}\right) \right] \tag{8}$$

where g is the acceleration of gravity, U is the wind speed at 10 meter above the sea level, a_0, a_1, and n are constants. ϕ is the azimuthal angle relative to the wind direction. The power p and the normalization constant N of the spread function are given by

$$p = p_0 + p_1 \left(U \sqrt{\frac{|k_b|}{g}}\right)^{p_2} \tag{9}$$

$$N = \frac{1}{4} \frac{\Gamma(p+1)}{\Gamma(p+\frac{1}{2})\,\Gamma(\frac{1}{2})} \tag{10}$$

where p_0, p_1, and p_2 are constants.

In the presence of long waves the backscatter will be modulated because the incidence angle is now to be measured relative to the local facet plane that is tilted by the long wave. This tilt modulation affects both β and F through k_b (refer (2), (5), and (6)). In addition hydrodynamic effects resulting from wave-wave interaction and differential wind forcing along the long wave profile act to modulate the backscatter by changing the short wave energy density at a fixed wavenumber.

- The first term represents the first order perturbation of the mapping factor β due to first order tilt perturbation of the incidence angle times the unperturbed short wave spectrum at the unperturbed Bragg wavenumber.
- The second term represents the first order change in the short wave spectrum due to a first order tilt perturbation of the Bragg wavenumber times the undisturbed mapping factor.

The first order hydrodynamic modulation is given by

$$\sigma_h^{(1)} = \beta(\theta^{(0)})\; F^{(1)}(\mathbf{k}^{(0)}) \qquad (17)$$

which is the first order perturbation of the short wave spectrum at a fixed wavenumber due to hydrodynamic modulation times the undisturbed mapping factor.

4.3 The second order terms

To second order, expansion of the backscatter gives;

$$\sigma^{(2)} = \sigma_t^{(2)} + \sigma_h^{(2)} + \sigma_{th}^{(2)} \qquad (18)$$

with the second order tilt modulation given by the sum

$$\begin{aligned}\sigma_t^{(2)} = {} & {\theta^{(1)}}^2 \frac{1}{2} \left.\frac{\partial^2 \beta}{\partial \theta^2}\right|_{\theta=\theta^{(0)}} F^{(0)}(\mathbf{k}^{(0)}) + \theta^{(2)} \left.\frac{\partial \beta}{\partial \theta}\right|_{\theta=\theta^{(0)}} F^{(0)}(\mathbf{k}^{(0)}) + \\ & \beta(\theta^{(0)})\, k_i^{(1)} k_j^{(1)} \frac{1}{2} \left.\frac{\partial^2 F^{(0)}}{\partial k_i \partial k_j}\right|_{\mathbf{k}=\mathbf{k}^{(0)}} + \\ & \beta(\theta^{(0)})\, k_i^{(2)} \left.\frac{\partial F^{(0)}}{\partial k_i}\right|_{\mathbf{k}=\mathbf{k}^{(0)}} + \theta^{(1)} \left.\frac{\partial \beta}{\partial \theta}\right|_{\theta=\theta^{(0)}} k_i^{(1)} \left.\frac{\partial F^{(0)}}{\partial k_i}\right|_{\mathbf{k}=\mathbf{k}^{(0)}} \end{aligned} \qquad (19)$$

where:

- The first term represents the second order perturbation of the mapping factor β due to first order tilt perturbation of the incidence angle times the unperturbed short wave spectrum at the unperturbed Bragg wavenumber.
- The second term is the first order perturbation of the mapping factor β due to second order tilt perturbation of the incidence angle times the unperturbed short wave spectrum at the unperturbed Bragg wavenumber.

The local facet normal vector which is pointing upwards, is given by

$$\mathbf{n} = \frac{\left(-\frac{\partial\zeta}{\partial x_1} , -\frac{\partial\zeta}{\partial x_2} , 1 \right)}{\sqrt{1 + \left(\frac{\partial\zeta}{\partial x_1}\right)^2 + \left(\frac{\partial\zeta}{\partial x_2}\right)^2}} \tag{23}$$

and the incidence angle relative to the local facet plane is given by

$$\cos\theta = - (\mathbf{n}\, \mathbf{e}) \tag{24}$$

where

$$\mathbf{e} = (\sin\theta^{(0)} , 0 , - \cos\theta^{(0)}) \tag{25}$$

is the unit vector, and $\theta^{(0)}$ is the unperturbed incidence angle of the emitted beam. $\theta^{(0)}$ is positive for a beam that is directed in the positive x_1 direction.

Expansion of (23) and (24) gives

$$\theta^{(1)} = - \frac{\partial\zeta^{(1)}}{\partial x_1} \tag{26}$$

$$\theta^{(2)} = - \frac{\partial\zeta^{(2)}}{\partial x_1} - \frac{1}{2} \operatorname{cotg}\theta^{(0)} \left(\frac{\partial\zeta^{(1)}}{\partial x_1}\right)^2 \tag{27}$$

The Bragg wavenumber is equal to minus twice the projection of the incident microwave wavenumber $\mathbf{k}_e$ onto the facet plane

$$\mathbf{k}_b = - 2 (\mathbf{k}_e - \mathbf{n} (\mathbf{k}_e\, \mathbf{n})) \tag{28}$$

which gives when expanding (omitting the subscript b)

$$k_1^{(0)} = - 2 \sin\theta^{(0)}\, k_e \tag{29}$$

$$k_1^{(1)} = 2 \cos\theta^{(0)}\, k_e \frac{\partial\zeta^{(1)}}{\partial x_1} \tag{30}$$

$$k_1^{(2)} = 2 \sin\theta^{(0)}\, k_e \left(\frac{\partial\zeta^{(1)}}{\partial x_1}\right)^2 + 2 \cos\theta^{(0)}\, k_e \frac{\partial\zeta^{(2)}}{\partial x_1} \tag{31}$$

as the Bragg wavenumber vector lies in the plane of incidence.

λ in (32) is a linear damping factor parameterizing the dissipation and wave-wave interaction. Here a formulation suggested by K. Hasselmann (personal communication) is used

$$\lambda(k_1^{(0)}) = \nu_{\mathrm{eff}}\, k_1^{(0)\,2} \tag{38}$$

where $\nu_{\mathrm{eff}} = O(10^{-4})$ is an effective constant of viscosity for these friction processes.

Assuming $F^{(1)}$ to be of the form

$$F^{(1)} = \sum_{0}^{\hat{\mathbf{k}}_{\mathrm{cut}}} A_F(\mathbf{k}, \hat{\mathbf{k}})\, \xi_{\hat{\mathbf{k}}} \exp(\, i\, \hat{\mathbf{k}}\, \mathbf{x} - i\, \hat{\omega}\, t\,) \; + \text{complex conjugate} \tag{39}$$

and insert it in (32), the following relation is found for A_F and its complex conjugate;

$$A_F = \Big[- k_1^{(0)} \hat{k}_1^{\,2} \frac{\hat{\omega}}{|\hat{\mathbf{k}}|}\, \omega\, \frac{\partial(\frac{F^{(0)}}{\omega})}{\partial k_1} \Bigg|_{\mathbf{k}=\mathbf{k}^{(0)}}$$

$$+ \alpha_1 (u_* \frac{\omega}{g})^{\alpha_2}\, \omega\, F^{(0)}\, |\hat{\mathbf{k}}| \exp(\, i\, \phi^{w}) \cos^2(\, \hat{\mathbf{k}}, \mathbf{k}\,) \Big] (\, \hat{\omega} + i\, \lambda\,)^{-1} \tag{40}$$

$$A_F^{*} = - A_F \tag{41}$$

The formulations of the wave-wave interaction term λ and the wind stress term $\hat{Y}$ above are quite uncertain. Therefore a computation of $F^{(2)}$, the second order spectral perturbation, seems not worthy. $F^{(2)}$ is put to zero for a start.

By inserting the long wave field (11) into the relations (26), (27), (30), and (31), and using the definition for the long wave spectrum $F(\hat{\mathbf{k}})$,

$$< \zeta^2 > = \sum_{0}^{\hat{\mathbf{k}}_{\mathrm{cut}}} F(\hat{\mathbf{k}}) = 2 \sum_{0}^{\hat{\mathbf{k}}_{\mathrm{cut}}} < |\xi_{\hat{\mathbf{k}}}|^2 > \tag{42}$$

the wave impact terms given in (19) and (21) can be expressed by the long wave spectrum.

The first of the second order tilt-hydrodynamic modulation terms becomes

$$< {}^1\sigma_{th}{}^{(2)} > = < \theta^{(1)} \left.\frac{\partial\beta}{\partial\theta}\right|_{\theta=\theta^{(0)}} F^{(1)}(\mathbf{k}^{(0)}) > = \frac{\partial\beta}{\partial\theta} \sum_{0}^{\hat{k}_{cut}} \Big[- i\, k_1^{(0)} \hat{k}_1{}^3 \frac{\hat{\omega}}{|\hat{\mathbf{k}}|}\, \omega \left.\frac{\partial(\frac{F^{(0)}}{\omega})}{\partial k_1}\right|_{\mathbf{k}=\mathbf{k}^{(0)}}$$

$$+ i\, \alpha_1 (u_* \frac{\omega}{g})^{\alpha_2} \omega\, F^{(0)}\, \hat{k}_1 |\hat{\mathbf{k}}| \exp(i\, \phi^w) \cos^2(\hat{\mathbf{k}}, \mathbf{k}) \Big] \frac{F(\hat{\mathbf{k}})}{(\hat{\omega} + i\, \lambda)} \qquad (49)$$

and the second term becomes

$$< {}^2\sigma_{th}{}^{(2)} > = < \beta(\theta^{(0)})\, k_1^{(1)} \left.\frac{\partial F^{(1)}}{\partial k_1}\right|_{\mathbf{k}=\mathbf{k}^{(0)}} >$$

$$= \beta\;\; 2\, k_e \cos\theta^{(0)} \sum_{0}^{\hat{k}_{cut}} \Big[i\, \hat{k}_1{}^3 \frac{\hat{\omega}}{|\hat{\mathbf{k}}|} \frac{\partial}{\partial k_1} [k_1^{(0)}\, \omega \left.\frac{\partial(\frac{F^{(0)}}{\omega})}{\partial k_1}\right|_{\mathbf{k}=\mathbf{k}^{(0)}} (\hat{\omega} + i\, \lambda)^{-1}]$$

$$- i\, \hat{k}_1 |\hat{\mathbf{k}}| \frac{\partial}{\partial k_1} [\alpha_1 (u_* \frac{\omega}{g})^{\alpha_2} \omega\, F^{(0)} \exp(i\, \phi^w) \cos^2(\hat{\mathbf{k}}, \mathbf{k}) (\hat{\omega} + i\, \lambda)^{-1}] \Big] F(\hat{\mathbf{k}}) \qquad (50)$$

The zeroth order term (14) and the seven second order wave modulation terms (43), and (45) through (50) make up the physical model function, WAMO, that takes care of the wave impact to the lowest order. It is summarized in table I.

5. Tuning of WAMO

WAMO should reduce to the Long C-band model (CMOD1, see Long, 1986) for the case of a fully developed windsea. In this case the long wave spectrum is given by the Pierson-Moskowitz spectrum

$$F(\hat{\mathbf{k}}) = F_{PM} = \frac{\gamma}{2} |\hat{\mathbf{k}}|^{-3} \exp(- 0.74 \frac{g^2}{U^4 |\hat{\mathbf{k}}|^2}) \frac{8}{3\pi} \cos^4\alpha \qquad (51)$$

where $\gamma = 0.0081$, and $-\frac{\pi}{2} \leq \alpha \leq \frac{\pi}{2}$ is the deviation from the downwind direction. F_{PM} is a function of only the local wind velocity U, so that WAMO becomes consistent with CMOD1 which also is only depending on U.

CMOD1 has the general form

$$\sigma = a + b_1 \cos\phi + b_2 \cos 2\phi \qquad (52)$$

Table I (continued)

Term	Definition	Interpretation	Expressed by the long wave spectrum, $F(\hat{k})$
$< {}^{4}\sigma_t^{(2)} >$	$< \beta\, k_1^{(2)} \frac{\partial F^{(0)}}{\partial k_1} >$	1. order change of the short wave spectrum due to 2. order tilt modulation of the Bragg wavenumber	$\beta \frac{\partial F^{(0)}}{\partial k_1}\ 2\, k_e \sin\theta^{(0)} \sum_{0}^{\hat{k}_{cut}} \hat{k}_1^{\,2} F(\hat{k})$
$< {}^{5}\sigma_t^{(2)} >$	$<\theta^{(1)} \frac{\partial \beta}{\partial \theta} k_1^{(1)} \frac{\partial F^{(0)}}{\partial k_1}>$	1. order change of the mapping factor times 1.order change of the short wave spectrum due to long wave slope	$-\frac{\partial \beta}{\partial \theta} \frac{\partial F^{(0)}}{\partial k_1}\ 2\, k_e \cos\theta^{(0)} \sum_{0}^{\hat{k}_{cut}} \hat{k}_1^{\,2} F(\hat{k})$
$< {}^{1}\sigma_{th}^{(2)}>$	$< \theta^{(1)} \frac{\partial \beta}{\partial \theta} F^{(1)}>$	1. order change of the mapping factor due to long wave slope times 1. order hydrodynamic modulation of the short wave spectrum	$\frac{\partial \beta}{\partial \theta} \sum_{0}^{\hat{k}_{cut}} \Big[-i\, k_1^{(0)} \hat{k}_1^{\,3} \frac{\hat{\omega}}{\lvert \hat{k} \rvert}\ \omega \frac{\partial(\frac{F^{(0)}}{\omega})}{\partial k_1} + i\, \alpha_1 (u_* \frac{\omega}{g})^{\alpha_2}$ $\omega\, F^{(0)}\ \hat{k}_1 \lvert \hat{k} \rvert \exp(i\, \phi^w) \cos^2(\hat{k}, k) \Big] \frac{F(\hat{k})}{(\hat{\omega} + i\, \lambda)}$

where a, b_1 , and b_2 are functions of the wind speed and the incidence angle, and ϕ is the azimuth angle between the radar beam and the wind direction.

A Fourier expansion to second order of WAMO will have the form

$$\sigma = \hat{a} + \hat{b}_1 \cos(\phi-\phi_1) + \hat{b}_2 \cos 2(\phi-\phi_2) \tag{53}$$

where $\hat{a}$, $\hat{b}_1$, and $\hat{b}_2$ are functions of the wind speed, the incidence angle, and the sea state which reduce to a, b_1 , and b_2 for fully developed windsea and ϕ_1 and ϕ_2 are functions of the wind speed, the incidence angle, and the sea state which become zero for fully developed windsea.

The Fourier coefficients of ϕ-expansion for WAMO's eight terms for fully developed windsea are given below.

For the zeroth term

$$ {}^{0}\hat{a} = \frac{1}{2\pi}\, \beta(\theta^{(0)})\; a k_1^{(0)\,-4} \tag{54}$$

$$ {}^{0}\hat{b}_1 = 0 \tag{55}$$

$$ {}^{0}\hat{b}_2 = \frac{4}{\pi}\, \beta(\theta^{(0)})\; a k_1^{(0)\,-4}\; N\, \gamma_0 \tag{56}$$

where a is given by (7), N by (10), and

$$\gamma_0 = \frac{\Gamma(\frac{1}{2})\,\Gamma(p+\frac{5}{2}) + \Gamma(\frac{5}{2})\,\Gamma(p+\frac{1}{2}) - 6\,\Gamma(\frac{3}{2})\,\Gamma(p+\frac{3}{2})}{\Gamma(p+3)} \tag{57}$$

where p is given by (9).

For the first tilt term

$$ {}^{t1}\hat{a} = \frac{1}{16}\left.\frac{\partial^2 \beta}{\partial \theta^2}\right|_{\theta=\theta^{(0)}} a k_1^{(0)\,-4}\; N\, D\, \gamma_1 \tag{58}$$

$$ {}^{t1}\hat{b}_1 = 0 \tag{59}$$

For the third tilt term

$$_{t3}\hat{a} = \frac{1}{4}\,\beta(\theta^{(0)})\,\left.\frac{\partial^2 (a k_1^{(0)\,-4} N)}{\partial k_1^2}\right|_{k=k^{(0)}} (\,k_e \cos\theta^{(0)}\,)^2\, D\,\gamma_1 \tag{67}$$

$$_{t3}\hat{b}_1 = 0 \tag{68}$$

$$_{t3}\hat{b}_2 = \frac{1}{2}\,\beta(\theta^{(0)})\,\left.\frac{\partial^2 (a k_1^{(0)\,-4} N)}{\partial k_1^2}\right|_{k=k^{(0)}} (\,k_e \cos\theta^{(0)}\,)^2\, D\,\gamma_2 \tag{69}$$

For the fourth tilt term

$$_{t4}\hat{a} = \frac{1}{4}\,\beta(\theta^{(0)})\,\left.\frac{\partial (a k_1^{(0)\,-4} N)}{\partial k_1}\right|_{k=k^{(0)}} k_e \sin\theta^{(0)}\; D\,\gamma_1 \tag{70}$$

$$_{t4}\hat{b}_1 = 0 \tag{71}$$

$$_{t4}\hat{b}_2 = \frac{1}{2}\,\beta(\theta^{(0)})\,\left.\frac{\partial (a k_1^{(0)\,-4} N)}{\partial k_1}\right|_{k=k^{(0)}} k_e \sin\theta^{(0)}\,)\; D\,\gamma_2 \tag{72}$$

For the fifth tilt term

$$_{t5}\hat{a} = -\,\frac{1}{4}\,k_e \cos\theta^{(0)}\,\left.\frac{\partial\beta}{\partial\theta}\right|_{\theta=\theta^{(0)}}\,\left.\frac{\partial (a k_1^{(0)\,-4} N)}{\partial k_1}\right|_{k=k^{(0)}} D\,\gamma_1 \tag{73}$$

$$_{t5}\hat{b}_1 = 0 \tag{74}$$

$$\text{th}2\hat{b}_2 = 0 \tag{83}$$

where

$$T_2 = \int_0^{\hat{k}_{cut}} -0.0081 \frac{4i}{3\pi} \Big[\sqrt{g\hat{k}}\ \ \frac{\partial}{\partial k_1}\{ k_1^{(0)}\ \omega \frac{\partial\left(\dfrac{a k_1^{(0)\ -4} N}{\omega}\right)}{\partial k_1} \Bigg|_{k=k^{(0)}} \ (\sqrt{g\hat{k}} + i\lambda)^{-1}]$$

$$- \frac{\partial}{\partial k_1}\{ \alpha_1 (u_* \frac{\omega}{g})^{\alpha_2} a k_1^{(0)\ -4} N\, \omega \exp(i\, \phi^w)\ (\sqrt{g\hat{k}} + i\lambda)^{-1}] \Big]$$

$$\exp(-0.74 \frac{g^2}{U^4 \hat{k}^2})\, d\hat{k} \tag{84}$$

Hence for fully developed windsea the zeroth order term together with the second order tilt terms contribute to the mean value $\hat{a}$ as well as to the second harmonic $\hat{b}_2$ in (53), while the hydrodynamic terms contribute to the first harmonic $\hat{b}_1$ only, see table II.

The ten constants a_0 , a_1 , and n in (7), p_0 , p_1 , and p_2 in (9), ϕ^w , α_1 , and α_2 in (35), and ν_{eff} in (38) may now be adjusted so that for a given set of values of wind speed, incidence angle, and azimuth angle WAMO's backscatter value gets equal to CMOD1's backscatter value. This is done by defining a cost function of the ten tuning parameters that has to be minimized over a given domain of wind speed, incidence angle, and azimuth angle.

It is convenient to use the Fourier coefficients of WAMO and CMOD1 when defining the cost function, firstly because the domain is then reduced to wind speed and incidence angle only, and secondly because it is then possible to give the harmonics different weight. (It is for example important that the mean values of WAMO and CMOD1 are equal, so that for a given wind speed and incidence angle the backscatter defined by WAMO and CMOD1 vary with the azimuth angle around the same level.) The cost function may then be written as

$$C = \int c_{U,\theta}\, dU\, d\theta \tag{85}$$

Table II (continued)

Term	Mean value, $\hat{a}$	First harmonic, $\hat{b}_1$	Second harmonic, $\hat{b}_2$
$< {}^4\sigma_t{}^{(2)} >$	$\frac{\beta}{4} \frac{\partial(a k_1^{(0)\,-4} N)}{\partial k_1} k_e \sin\theta^{(0)}\, D\, \gamma_1$	0	$\frac{\beta}{2} \frac{\partial(a k_1^{(0)\,-4} N)}{\partial k_1} k_e \sin\theta^{(0)}\, D\, \gamma_2$
$< {}^5\sigma_t{}^{(2)} >$	$- \frac{k_e}{4} \cos\theta^{(0)} \frac{\partial\beta}{\partial\theta} \frac{\partial(a k_1^{(0)\,-4} N)}{\partial k_1} D\, \gamma_1$	0	$- \frac{k_e}{2} \cos\theta^{(0)} \frac{\partial\beta}{\partial\theta} \frac{\partial(a k_1^{(0)\,-4} N)}{\partial k_1} D\, \gamma_2$
$< {}^1\sigma_{th}{}^{(2)} >$	0	$\frac{128}{35\pi} \frac{\partial\beta}{\partial\theta} T_1\, \gamma_3$	0
$< {}^1\sigma_{th}{}^{(2)} >$	0	$\frac{256}{35\pi} k_e \cos\theta^{(0)}\, \beta(\theta^{(0)})\, T_2\, \gamma_3$	0

(See text for the definition of parameters.)

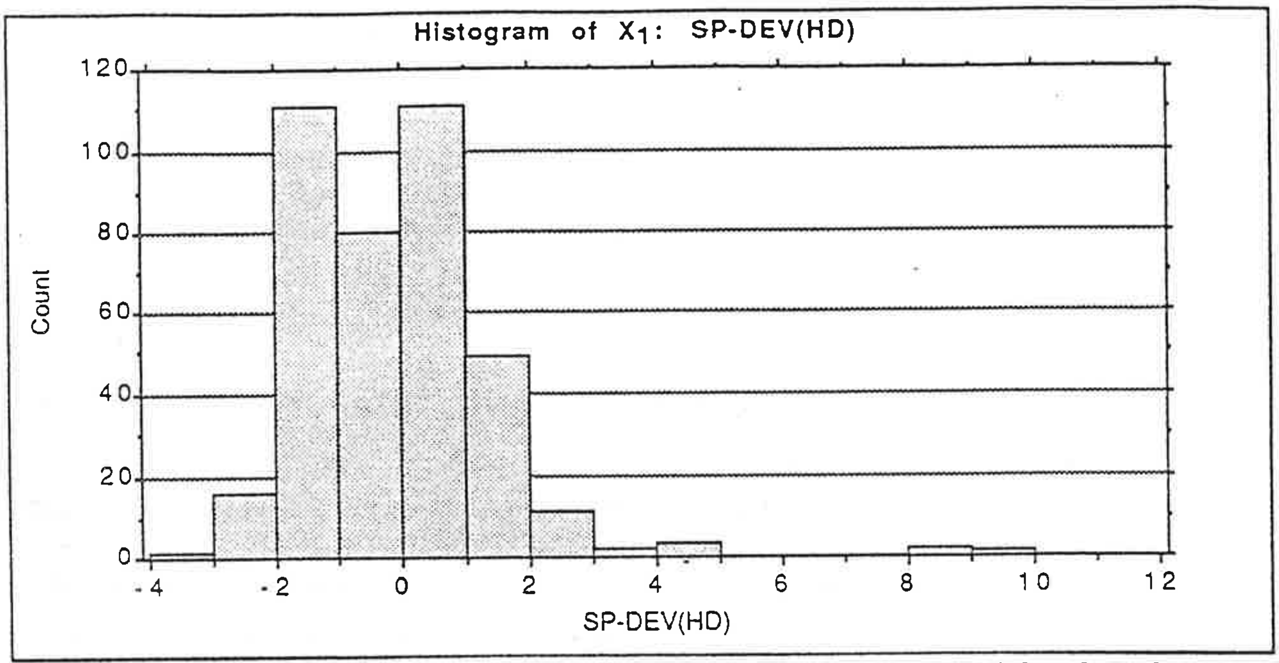

Figure 1a Speed deviation retrieved with WAMO(HD) in the half developed windsea case.

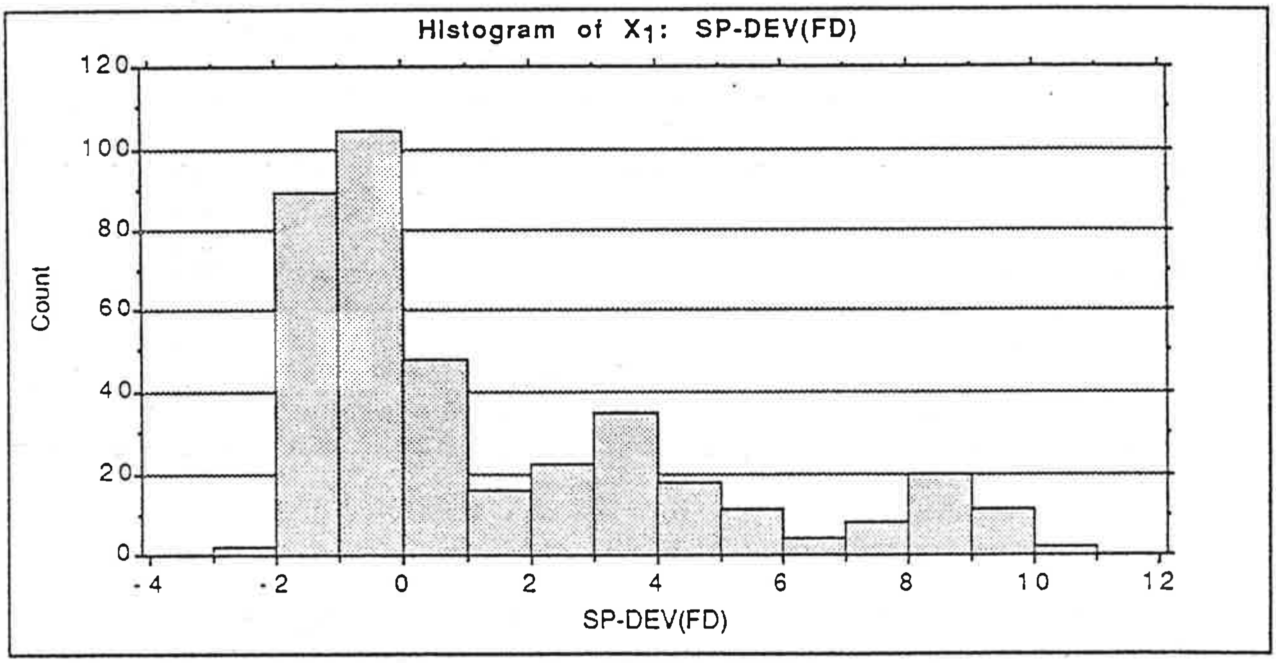

Figure 1b Speed deviation retrieved with WAMO(FD) in the half developed windsea case.

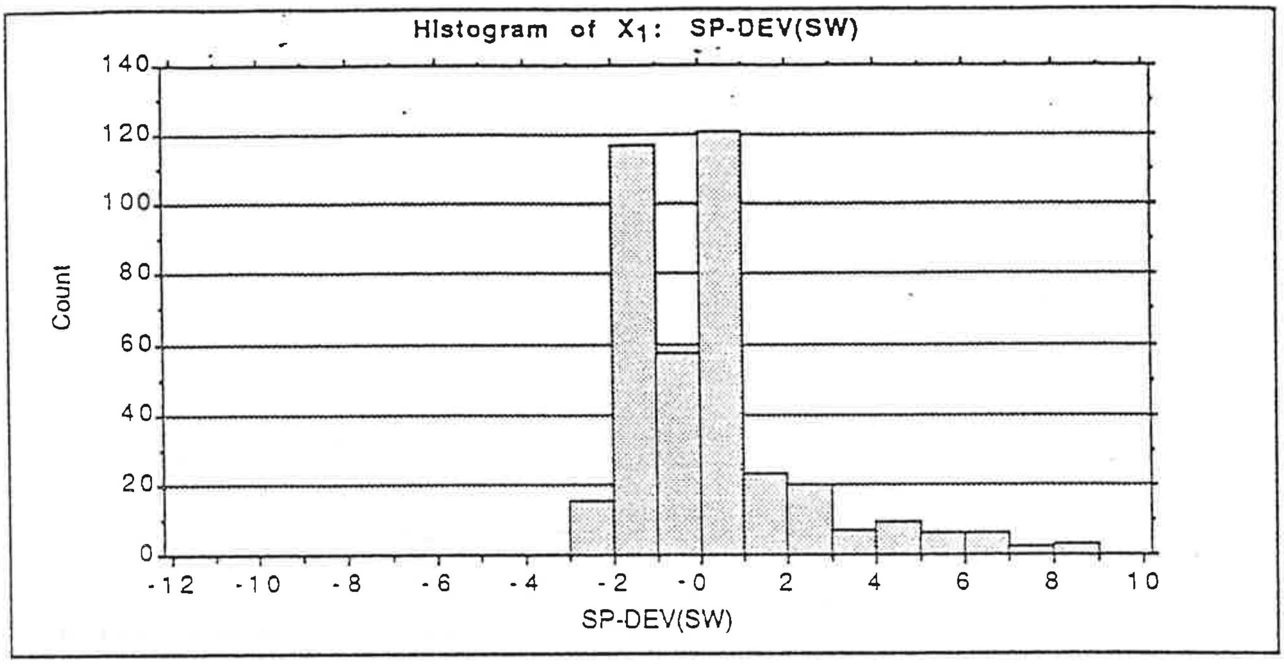

Figure 2a Speed deviation retrieved with WAMO(SW) in the swell case.

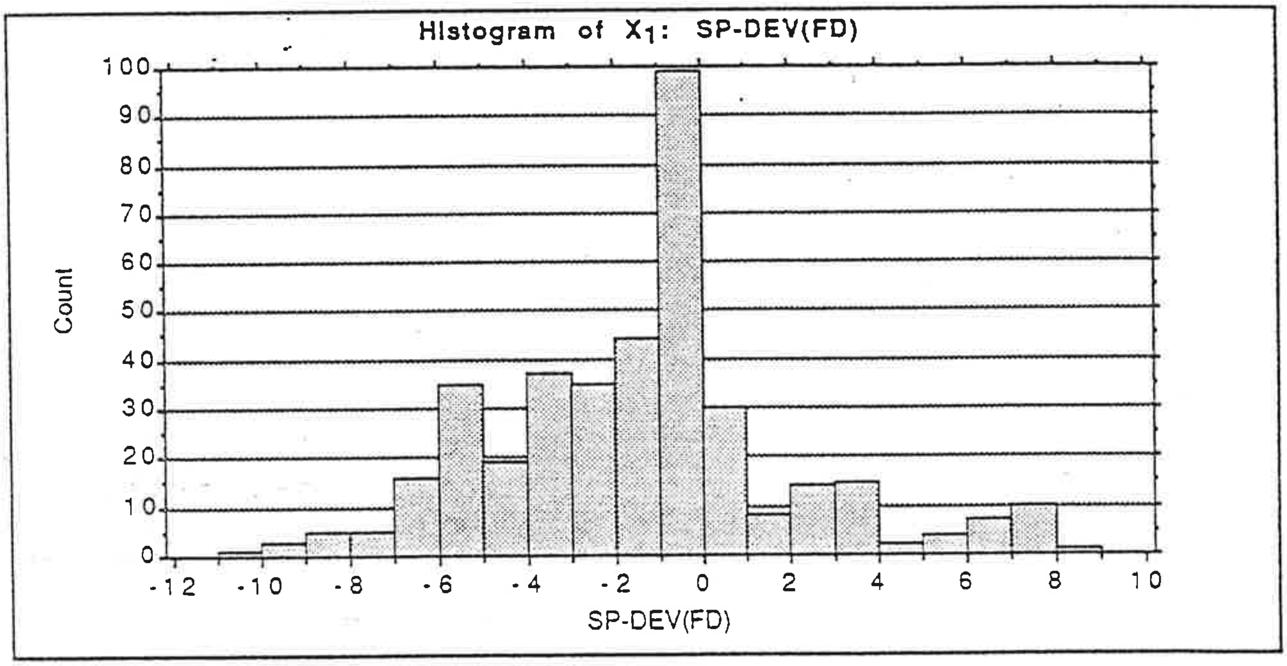

Figure 2b Speed deviation retrieved with WAMO(FD) in the swell case.

in the model. The mean backscatter then consists of a zeroth order unmodulated term and seven second order wave modulated terms that are expressed by the long wave spectrum. Hence the mean backscatter is a function of wind speed, azimuth angle between wind direction and radar beam, incidence angle, and sea state.

For a long wave spectrum representing fully developed windsea and no swell, Fourier expansion with respect to the azimuth angle reveals that the zeroth term and the second order tilt terms contribute to the mean value as well as to the second cosine harmonic, while the second order tilt-hydrodynamic terms contribute to the first cosine harmonic only. In the case of fully developed windsea the long wave spectrum (Pierson-Moskowitz spectrum) is only dependent on the wind velocity, and the backscatter value for an arbitrary set of wind speed, azimuth angle, and incidence angle should agree with the value given by the empirical C-band model CMOD1, which is independent on the sea state. This is achieved by tuning some constants appearing in the short wave spectrum formulation, and in the formulation of the hydrodynamic modulation. The tuning is still in process, as there is need of refining the behaviour of the model at low and high incidence angles and low and high wind speeds.

Some preliminary testing of the wave impact has been done by inserting long wave spectra for half developed windsea and for swell in the model, and use it in a forward sense to produce simulated backscatter values. Thereafter a wind retrieval algorithm has been applied, where in one case the model function was specific for the sea state and in another case the model function was independent of the sea state. The wave impact was demonstrated by the larger deviations in the retrieved winds from the true winds, when the model function was independent of the sea state.

The preliminary tests of the wave impact on the scatterometer wind retrieval with the physical model function are promising, and the work on refining the model further should be feasible.

On an operational basis the procedure of including the wave information has to be optimized. The wind algorithm has to extend its structure to take care of the additional wave information which is provided by a wave forecasting model. There are no severe obstacles in making this extension streamlined and effective.

8. References

Donelan, M.A., and W.J.Pierson, *Radar Scattering and Equilibrium Ranges in Wind-Generated Waves With Application to Scatterometry.*
J.Geophys.Res., 92, C5, 4971-5029, 1987.

Feindt, F., *Radar - Rückstreuexperimente am Wind-Wellen-Kanal bei sauberer und filmbedeckter Wasseroberfläche im X-Band (9.8 GHz).*
Hamburger Geophysikalische Einzelschriften, Reihe A, Heft 75, 1985.

Gill, P.E., and W. Murray, *Conjugate-gradient Methods for Large-scale Nonlinear Optimization.*
Dept. of Operations Research, Stanford University, Tech, Rep. SOL 79-15, 1979.